ISSN 0915-633X

NATIONAL INSTITUTE FOR FUSION SCIENCE

MHD Equilibrium and Stability in Heliotron Plasmas

K. Ichiguchi

(Received - Aug. 18, 1999)

NIFS-611 Sep. 1999

RESEARCH REPORT
NIFS Series

NAGOYA, JAPAN

MHD Equilibrium and Stability in Heliotron Plasmas

Katsuji ICHIGUCHI
National Institute for Fusion Science, Toki 509-5292, Japan
e-mail : ichiguch@nifs.ac.jp
(submitted to 'Recent Research Development in Plasmas')

Abstract

Recent topics in the theoretical magnetohydrodynamic (MHD) analysis in the heliotron configuration are overviewed. Particularly, properties of three-dimensional equilibria, stability boundary of the interchange mode, effects of the net toroidal current including the bootstrap current and the ballooning mode stability are focused.

Key Words : heliotron, MHD, three-dimensional equilibrium, interchange mode, net toroidal current, bootstrap current, internal kink mode, external kink mode, ballooning mode.

1 Introduction

In the magnetic confinement of the fusion plasma, the most successful experimental data have been obtained in the large tokamaks. Particularly, in the tokamaks such as the JET[1] and the TFTR[2], DT experiments were carried out and the essential data of burning plasma were obtained which will be inevitable in the design of the devices of the next step such as ITER[3]. In order to confine high temperature plasma in toroidal systems, nested magnetic surfaces are necessary corresponding to the existence of magnetohydrodynamic (MHD) equilibrium. A large toroidal plasma current is driven to generate a poloidal magnetic field to construct the magnetic surfaces in the tokamaks. However, existence of such a plasma current in the tokamaks potentially has a possibility of the disruptive instability, which releases almost all energy in a short time on the order of 0.1msec. Another difficulty concerning with the current is that a non-inductive current drive is required to realize a continuous operation of tokamaks.

From the point of the continuous operation without the disruption, the stellarator configuration is one of the alternative promising approaches. In this review, the term of 'stellarator' is used for every configuration in which the nested magnetic surfaces and the rotational transform are produced by external coil-currents. That is, in the stellarators the global plasma current is not necessary in the plasma confinement. The heliotron configuration is one of the stellarator concepts which is characterized by the continuous helical windings. The original concept of the heliotron was invented by Uo[4]. He proposed a so-called poloidal heliotron at first, and later, modified his idea to a heliotron with continuous helical windings. The main difference from the classical stellarator is that the currents in the helical windings flow in the same direction. Therefore, the structure of the heliotron device is simple compared with the classical stellarators because the number of the helical windings is half of that of the corresponding classical stellarator and the toroidal field coils are not needed. Instead, vertical field coils are necessary in generation of the nested surfaces; however, they can be used for the extension of the flexibility of the configuration.

The feasibility to the confinement of the fusion plasma was firstly shown in Heliotron D device in Plasma Physics Laboratory, Kyoto University[5] which has two helical windings ($\ell = 2$). After that, heliotron devices with $\ell = 2$ were constructed in sev-

eral laboratories in the world. The heliotron project in Kyoto University was succeeded by the Heliotron DR (H-DR)[6] and the Heliotron E (H-E)[7] devices. The ATF[8], the URAGAN-2M[9] and the CHS[10] devices were constructed, in Oak Ridge National Laboratory, Kharkov institute of Physics and Technology and Institute Plasma Physics Nagoya Unversity, respectively. The coil parameters of these devices are summarized in Table 1. In these devices, the plasma

Table.1 Coil parameters of recent heliotron devices.

	H-DR	H-E	ATF	CHS	LHD
R_0(m)	0.9	2.2	2.1	1	3.9
a_c(m)	0.135	0.293	0.46	0.313	0.975
N_T	15	19	12	8	10
M_P	1	3	3	4	3

R_0:Major radius of helical windings, a_c:Minor radius of helical windings, N_T:Number of field period, M_P:Number of pairs of poloidal field coil

with a few keV of ion temperature, the density in the order of $10^{20}m^{-3}$ and the average beta value of 2% were achieved[11]. Thus, the heliotron configuration is considered as one of the most hopeful alternative configurations in the magnetic confinement of fusion plasmas. After these successful experiments, the Large Helical Device (LHD) was constructed in the National Institute for Fusion Science (NIFS)[12, 13], and the experiment started in 1998[14]. The LHD is the largest heliotron device with superconducting coils for the steady state operation. Many theoretical analyses in heliotron configurations has been progressed through the design and the construction of the LHD intensively. Hence, some of the topics in this review are concerned with the research of the LHD configuration.

In the many operations in the above heliotron devices, global MHD fluctuations which almost limits the achievable beta value were observed. Particularly, in the Heliotron E high-beta experiments, sawtooth-like fluctuations and internal disruptions in the soft X-ray measurement which had coincidence with magnetic fluctuations[15]. At the internal disruption, 20 $\sim$ 30% of plasma energy is lost by the enhancement of the energy and particle transport. Thus, it has been crucial to understand the mechanism of such instabilities theoretically and to know what kind of configuration is favorable for the high performance plasmas in the heliotron configurations.

Since there is no geometrical symmetry in the heliotron configuration, the theoretical analysis has to be essentially three-dimensional. However, it is not easy to treat the three-dimensional plasma as it is. Hence, various approximations have been considered in the study of MHD equilibria and stability. The first successful approximation was the stellarator expansion method developed by Greene and Johnson[16]. This approach is based on the so-called stellarator ordering and the averaging the helical equilibrium quantities in the toroidal direction. The stellarator ordering consists of the following two essential ideas with respect to a small parameter $\epsilon \equiv a/R << 1$, where a and R are the minor and the major radii of the plasma, respectively. One is that the ratio of the helical component of the magnetic field to the uniform toroidal component is in the order of $\epsilon^{1/2}$, and the other is that the ratio of the plasma pressure to the magnetic pressure, which is called the beta value, is in the order of ϵ. Applying the stellarator ordering to the MHD equilibrium equations, a two-dimensional Grad-Shafranov type equation can be derived for heliotron plasmas. The stellarator ordering was also applied to the energy principle[17] for the linear ideal stability of the equilibrium obtained from the Grad-Shafranov type equation[18]. In the stability analysis with this technique, the stability is examined as a two-dimensional eigenvalue problem.

On the other hand, the initial value approach based on the reduced MHD equations has been successfully developed for the stability analysis in the heliotron configuration. This approach was originally developed for the stability of the tokamak plasma. By using the high-beta ordering of $\beta \sim \epsilon$, the incompressible MHD equations for tokamaks can be reduced to the three-field equations for poloidal magnetic flux, stream function and plasma pressure. Strauss[19] employed the stellarator ordering in the reduction process of the MHD equations and applied the averaging method for the helical variations to obtain the three-field equations for stellarators. By dropping both the time derivative and the stream function from these reduced MHD equations, the same Grad-Shafranov type equation as derived by Greene and Johnson can be reproduced for the static equilibrium. The quadratic form for the linear ideal perturbation derived from the reduced equations is also similar to the energy principle in the stellarator expansion method in principle. Therefore, the reduced equations derived

by Strauss are equivalent to the stellarator expansion method in the static equilibrium and the linear ideal stability.

It is noted that both approaches of the stellarator expansion method and the reduced MHD equations can examine the three-dimensional equilibrium and stability by means of the two-dimensional technique. The stability analysis using the stellarator expansion method based on the energy principle has an advantage that the vacuum contribution for the external modes can be included straightforward. On the contrary, the approach utilizing the reduced equations can treat the non-ideal effect such as resistivity, and it is easy to extend the numerical scheme to the nonlinear analysis because the equations are usually solved as an initial value problem. Thus, several stability code has been developed based on both methods[20, 21, 22, 23]. Furthermore, various approaches has been proposed to include higher order effects, particularly, the toroidicity effects[24, 25, 26, 27], because the classical stellarator ordering cannot give a good approximation for recent medium or small aspect ratio heliotrons.

In order to study the stability with these two-dimensional scheme, the equilibrium to be examined have to be expressed in the two-dimensional form consistent with the ordering in the stability scheme. Previously, the Grad-Shafranov type equation was solved numerically to obtain the two-dimensional expression of the equilibrium. On the other hand, the effort for the numerical scheme to obtain the three-dimensional equilibrium without any ordering has been also developed. Firstly, the BETA code[28, 29] was succeeded in solving the three-dimensional equilibrium with Lagrangian coordinates. Since the code employed the finite difference method for the derivatives in the poloidal and the toroidal coordinates as well as in the radial coordinate, many grids were needed in every direction to obtain a good numerical accuracy. After that, Hirshman et al. developed the VMEC code[30, 31] with the spectral method in both poloidal and toroidal directions in a Lagrangian coordinates. This code is very useful in the point of the computer resource, and therefore, is almost the standard code in the three-dimensional MHD equilibrium calculation these days.

Since a three-dimensional equilibrium can be obtained numerically by utilizing the VMEC code, numerical schemes to examine the VMEC results with two-dimensional approach have been developed[32, 33, 34, 35]. In these schemes, interface codes to generate two-dimensional equilibrium quantities from the three-dimensional solution are provided. The results of several benchmark test of the numerical stability codes in this type are summarized in Ref.[36]. Good agreements among them are shown. Recently, stability codes with a three-dimensional technique are also developed[37, 38]. These codes are based on the energy principle and do not employ any ordering or averaging method. Hence, they are very useful in the stability analysis where the three-dimensional effect is essential.

The VMEC code is based on the assumption of the existence of nested surfaces in the equilibrium. However, in the three-dimensional configurations, there is no mathematical proof for the assumption, and magnetic islands and stochastic region can exist in the plasma confinement region. In order to study the effects of the islands and the stochastic region to the MHD equilibrium, three-dimensional equilibrium codes employing the Eulerian coordinates has been developed. Recently, two codes has been successfully developed independently to study the destruction of the magnetic surfaces[39, 40]. They give interesting results concerning with destruction of the nested surfaces due to the finite beta effects.

In this review paper, we overview recent progress in the study of the MHD equilibrium and stability in the heliotron configurations which are obtained with the approaches mentioned above. The advance of the MHD study in this decade is owing to the fact that a three-dimensional equilibrium can be calculated easily. Thus, the properties and the stability of the three-dimensional equilibrium are mainly focused here. This paper is composed as follows. In Section 2, the numerical approaches often used in the equilibrium and the stability analysis for the heliotron plasmas are briefly explained. In Section 3, recent topics studied with the approaches explained in Section 2 are discussed. The properties of the three-dimensional equilibrium analysis are shown in Sec.3.1 firstly. After that the stability of the equilibrium against the interchange mode is discussed in Sec.3.2, as the mode is the most crucial instability in the heliotron plasma and therefore, examined widely. Because a net toroidal current can flow even in the heliotron plasma, the investigation of the effects of the current are reviewed in Sec.3.4. The influence on the interchange mode and the current driven mode are presented. The bootstrap current in the heliotron

plasma is discussed as one of the net current. Recently, it is found that the ballooning mode is also destabilized in the heliotron plasmas. The mechanism of the mode is discussed and the properties are presented in Sec.3.5. The comparison between the theoretical and the experimental results are shown in Section 4 in several devices to show how well the theoretical approach can explain the experimental data. Summary is given in Section 5.

2 Numerical Scheme of the MHD Analysis in Heliotron Configuration

2.1 Equilibrium calculation

2.1.1 VMEC code

The existence of the three-dimensional MHD equilibrium with nested surfaces has not been proved mathematically. If the region of the magnetic island or the stochastic region is narrow enough, however, the assumption of the existence of the 3D equilibrium with the nested surfaces would be approximately valid. Kruskal and Kulsrud[41] showed that the first variation of the internal energy W_P given by

$$W_P = \int_P \left(\frac{B^2}{2\mu_0} + \frac{P}{\Gamma - 1} \right) dV \tag{2.1}$$

gives the equilibrium equation,

$$\nabla P = \boldsymbol{J} \times \boldsymbol{B}, \tag{2.2}$$

where $\boldsymbol{B}$, $\boldsymbol{J}$ and P denote the magnetic field, the the current density and the plasma pressure, respectively. μ_0 and Γ are the permeability in vacuum and the specific heat of the plasma, respectively, and $\int_P dV$ means the volume integral in the plasma region.

According to their theorem, the equilibrium problem can be written in the Lagrangian coordinates. In this case, the radial coordinate is characterized by the flux surfaces at the finite beta equilibrium, and the equilibrium is determined by solving the equation for the spatial position of each flux surface. The numerical scheme employing this idea is called an inverse solver. The most convenient inverse solver is the VMEC code developed by Hirshman et al.[30, 31].

In the VMEC code, the cylindrical coordinates of the flux surface (R, ϕ, Z) are solved as the functions of flux coordinates (s, θ, ζ), where s denotes the normalized toroidal magnetic flux and θ and ζ are the poloidal and the toroidal angles, respectively. The toroidal angle ζ is taken as the same as ϕ. The poloidal angle θ is given by

$$\theta^* = \theta + \lambda(s, \theta, \zeta), \tag{2.3}$$

where θ^* is the poloidal angle with which the magnetic field line is expressed as a straight line. Here, λ is a periodic function of θ and ζ, which is introduced to give a freedom of the poloidal angle. The spectral method is employed in the VMEC code so that the cylindrical variables are expressed as

$$R(s, \theta, \zeta) = \sum_{m,n} R_{mn}(s) \cos(m\theta + n\zeta) \tag{2.4}$$

$$Z(s, \theta, \zeta) = \sum_{m,n} Z_{mn}(s) \sin(m\theta + n\zeta) \tag{2.5}$$

$$\lambda(s, \theta, \zeta) = \sum_{m,n} \lambda_{mn}(s) \sin(m\theta + n\zeta). \tag{2.6}$$

The solution of the equilibrium is given by the Fourier components, R_{mn}, Z_{mn} and λ_{mn}.

The first variation of W_P with respect to the Fourier components is written as

$$\frac{dW_P}{dt} = \int_P \sum_{m,n} \left(F_{Rmn} \frac{dR_{mn}}{dt} + F_{Zmn} \frac{dZ_{mn}}{dt} + F_{\lambda mn} \frac{d\lambda_{mn}}{dt} \right) dV. \tag{2.7}$$

Here the variation is represented by the virtual time derivative which corresponds to the numerical iteration. The equilibrium can be obtained when $dW_P/dt = 0$ which is given by the vanishment of the residual forces, $F_{imn} = 0$ $(i = R, Z, \lambda)$.

In the numerical iteration scheme, the monotonous convergence to the equilibrium should be guaranteed. This condition is achieved by taking the descent path of the iteration as

$$\frac{dR_{mn}}{dt} = -F_{Rmn}, \quad \frac{dZ_{mn}}{dt} = -F_{Zmn}, \quad \frac{d\lambda_{mn}}{dt} = -F_{\lambda mn}. \tag{2.8}$$

In the VMEC code, the second order Richardson method is employed to accelerate the convergence.

It is noted that the three equations of the residual force for R, Z and λ are dependent. It is one of the most remarkable points in the VMEC code how to avoid the dependence of the equations. As the freedom of the poloidal angle is taken into account by introducing λ in the formulation, a constraint to

ensure the rapid convergence of the Fourier series can be imposed to obtain independent equations[42]. If we introduce a function of the power spectrum of R and Z defined by

$$M = \frac{\sum_{m\geq 1} m^{p+1} S_m}{\sum_{m\geq 1} m^p S_m} \quad (p > 1), \tag{2.9}$$

where

$$S_m = \sum_n (R_{mn}^2 + Z_{mn}^2), \tag{2.10}$$

the minimization of M leads to the condensation of the R and Z spectra toward low poloidal mode numbers. Thus, the independent Euler equations under the constraint of the rapid convergence of poloidal mode number can be obtained by the minimization of $W_P + \alpha M$ instead of W_P with respect to R, Z and λ, where α is a normalization parameter concerning with the residual forces.

The equilibrium under the fixed boundary condition can be solved by means of above scheme with the information of the boundary shape and the profiles of the pressure (or the mass) and the net toroidal current (or the rotational transform). On the contrary, in the case of the free boundary condition, the magnetic field in the vacuum region has to be solved as well as that in the plasma region. In this case, the variation of energy functional including the part of vacuum region defined by

$$W = W_P - W_V$$
$$= \int_P \left(\frac{B^2}{2\mu_0} + \frac{P}{\Gamma - 1} \right) dV - \int_V \frac{|\nabla \phi_V|^2}{2\mu_0} dV \tag{2.11}$$

is utilized, where ϕ_V is the vacuum magnetic potential and $\int_V dV$ means the volume integral in the vacuum region. The Euler equation in the plasma region corresponds to the force balance equation again. The variation with respect to ϕ_V in the vacuum region gives the Laplace's equation,

$$\nabla^2 \phi_V = 0 \tag{2.12}$$

and the pressure balance equation at the plasma vacuum interface

$$\frac{B^2}{2\mu_0} + P = \frac{|\nabla \phi_V|^2}{2\mu_0}. \tag{2.13}$$

The Green's function is employed in solving the Laplace's equation in the VMEC code.

2.1.2 HINT and PIES codes

Recently, two equilibrium codes which can solve the equilibria including magnetic islands or stochastic region in the plasma column without any assumption of the existence of the nested surfaces have been successfully developed. One is the HINT code[39] and the other is the PIES code[40].

In the HINT code, a special type of Eulerian coordinates is employed in order to save the memory of the computation. In the coordinates, the poloidal cross section on which the rectangular grids are spanned rotates in the toroidal direction with the same pitch as that of the external coil. The HINT code solves the three-dimensional equilibrium by means of the time-dependent relaxation method on the coordinates. This method is composed of the two steps. In the first step, the condition of

$$\boldsymbol{B} \cdot \nabla P = 0 \tag{2.14}$$

is achieved by the time evolution of the equation set for the artificial parallel sound wave,

$$\frac{\partial P}{\partial t} = \boldsymbol{B} \cdot \nabla \boldsymbol{v}_s \tag{2.15}$$

$$\frac{\partial \boldsymbol{v}_s}{\partial t} = \boldsymbol{B} \cdot \nabla P. \tag{2.16}$$

The magnetic field $\boldsymbol{B}$ is fixed during the first step. The uniform pressure along the field line is obtained by setting the artificial kinetic energy $K_s = \int v_s^2 dV$ to zero when K_s reaches a maximum value in the time evolution. This procedure is repeated several times in the first step. The second step is another time evolution of the following equations,

$$\frac{\partial \rho_m \boldsymbol{V}}{\partial t} = -\nabla \cdot \left[P\mathbf{I} - \left(\boldsymbol{B}\boldsymbol{B} - \frac{1}{2} B^2 \mathbf{I} \right) \right] + \nu_a \nabla^2 \boldsymbol{V} \tag{2.17}$$

$$\frac{\partial \boldsymbol{B}}{\partial t} = \nabla \times (\boldsymbol{V} \times \boldsymbol{B} - \eta_a \boldsymbol{J}) \tag{2.18}$$

$$\boldsymbol{J} = \nabla \times \boldsymbol{B}, \tag{2.19}$$

where ρ_m is the mass density and $\mathbf{I}$ denotes a unit dyadic. ν_a and η_a are the artificial viscosity and resistivity, respectively. In this step, the pressure P is fixed. Thus, the magnetic field is obtained which satisfies $\boldsymbol{J} \times \boldsymbol{B} = \nabla P$ for a given pressure profiles when the artificial velocity $\boldsymbol{V}$ is relaxed to be zero. By iterating these steps, a consistent three-dimensional equilibrium can be solved.

In the PIES code, the procedure to obtain a three-dimensional equilibrium is composed of the following four steps. At first, the pressure P is chosen so that the pressure is constant along the given field line to satisfy the condition,

$$\boldsymbol{B} \cdot \nabla P = 0. \tag{2.20}$$

In the second step, the current component perpendicular to the magnetic field $\boldsymbol{J}_\perp$ is obtained by

$$\boldsymbol{J}_\perp = \frac{\boldsymbol{B} \times \nabla P}{B^2}. \tag{2.21}$$

In the next step, the Pfirsch-Schlüter current is obtained by solving the magnetic differential equation

$$\boldsymbol{B} \cdot \nabla \left(\frac{\boldsymbol{J} \cdot \boldsymbol{B}}{B^2} \right) = -\nabla \cdot \boldsymbol{J}_\perp, \tag{2.22}$$

which is given by the divergence free condition for $\boldsymbol{J}$. At last, the magnetic field is updated by the solution of the Ampère's law

$$\nabla \times \boldsymbol{B} = \boldsymbol{J}. \tag{2.23}$$

By iterating above procedure, the consistent solution for three-dimensional equilibrium can be obtained without any assumption of the nested surfaces. As the equilibrium may involve the magnetic islands and the stochastic region, the field lines are traced at each iteration to construct a quasi-magnetic coordinates (ψ, θ, ϕ) with which the magnetic field is expressed as

$$\boldsymbol{B} = \nabla\psi \times \nabla\theta + \iota \nabla\phi \times \nabla\psi + \boldsymbol{b}, \tag{2.24}$$

where ι denotes the rotational transform. Here, $\boldsymbol{b}$ is introduced in order to avoid the singularity in the magnetic differential equation. Thus, it is very small in the region of the nested surfaces. In the region with the magnetic islands and the stochastic region, the quasi-magnetic coordinates are extrapolated so as to connect the coordinates in the region of the nested surfaces.

2.1.3 Two-dimensional approach

The numerical schemes which can examine the three-dimensional equilibrium with two dimensional technique have been developed extensively. Especially, the KSTEP , the TWIST, the RESORM and the CHAFAR codes are developed to study the linear stability of the equilibrium calculated with the VMEC code. In the two dimensional approach of the stability analysis, there are two kinds of numerical code. One is the group which utilizes the energy principle and the other one utilizes the reduced MHD equations. The growth rate of the mode is solved as an eigenvalue problem in the former case and as an initial value problem in the latter case. The KSTEP and the TWIST codes belongs to the former category and the RESORM and the CHAFAR codes to the latter one. Here we focus on the KSTEP code and the RESORM code because thy are used frequently for the stability of heliotron plasmas.

The most representative code in the former group is the KSTEP code[32]. The code was originally developed, which is called STEP[22], by applying the stellarator expansion method to the PEST code[43] which was used in the tokamak stability analysis. After that it has been modified so as to include higher order correction in the inverse aspect ratio to relax the limitation of the large aspect ratio, and the interface code as the connection to the VMEC code has been provided[27]. In this code, the displacement vector perpendicular to the equilibrium field is given by

$$\boldsymbol{\xi}_\perp = \frac{R^2}{R_0^2} \nabla\zeta \times \nabla\Phi, \tag{2.25}$$

where R and Φ denote the major radius and the stream function, respectively. The KSTEP code solves the eigenvalue and the eigenfunction of the Lagrangian given by

$$\begin{aligned} L = & \quad \omega^2 \int d\tau \rho_m \frac{|\nabla\Phi|^2}{R^2} \\ & - \int d\tau \left\{ |\boldsymbol{Q}_\perp|^2 + \frac{R_0 B_0 \boldsymbol{J} \cdot \boldsymbol{B}}{R^2 B^2} \boldsymbol{Q}_\perp \cdot \nabla\Phi^* \right. \\ & \left. + \boldsymbol{\xi}_\perp \cdot \nabla P \boldsymbol{\xi}_\perp^* \cdot \nabla\Omega \right\} \end{aligned} \tag{2.26}$$

with

$$\boldsymbol{Q}_\perp = \nabla\zeta \times \nabla[(R_0 B_0 \nabla\zeta + \nabla\zeta \times \nabla\Psi_{eq}) \cdot \nabla\Phi], \tag{2.27}$$

where ζ denotes the toroidal angle. The subscript 0 means the value at the magnetic axis and Ψ_{eq} denotes the equilibrium poloidal flux. The averaged magnetic curvature, Ω, is given by

$$\Omega = \frac{N}{2\pi} \int_0^{2\pi/N} d\zeta \left(\frac{R}{R_0} \right)^2 \left(1 + \frac{|\boldsymbol{B} - \overline{\boldsymbol{B}}|^2}{B_0^2} \right), \tag{2.28}$$

where $\overline{\boldsymbol{B}}$ denotes the axisymmetric part of the magnetic field. The first and the second terms in the

integrand correspond to the toroidal and the helical components of the field line curvature, respectively. The parallel current in eq.(2.26) is given by

$$\frac{\boldsymbol{J}\cdot\boldsymbol{B}}{B^2} = -\frac{dP}{d\Psi_{eq}}\Omega + G(\Psi_{eq}) \tag{2.29}$$

in the ordering. G is a flux function determined by the condition for the net toroidal current in the equilibrium. In the free boundary case, the vacuum integral term is added to the Lagrangian, which is represented by the Green's function. These two-dimensional equilibrium quantities are calculated from the three-dimensional VMEC solution.

The reduced MHD equations for the stellarators were originally derived by Strauss[19]. He utilized an averaging method based on the stellarator ordering to derive the equations for the poloidal magnetic flux Ψ, the stream function Φ and the plasma pressure P. Ichiguchi et al.[26] derived the modified three field equations by including the higher order corrections in the toroidicity which is similar ones employed in the KSTEP code, given by

$$\frac{\partial\Psi}{\partial t} = -\left(\frac{R}{R_0}\right)^2 \boldsymbol{B}\cdot\nabla\Phi + \eta\nabla_\perp^2\Psi, \tag{2.30}$$

$$\rho_m\frac{d\nabla_\perp^2\Phi}{dt} = -\boldsymbol{B}\cdot\nabla\nabla_\perp^2\Psi + R_0^2\nabla\Omega\times\nabla P\cdot\nabla\zeta \tag{2.31}$$

and

$$\frac{dP}{dt} = 0. \tag{2.32}$$

The magnetic differential operator and the convective time derivative are written as

$$\boldsymbol{B}\cdot\nabla = \frac{R_0B_0}{R^2}\frac{\partial}{\partial\zeta} - \nabla\Psi\times\nabla\zeta\cdot\nabla \tag{2.33}$$

and

$$\frac{d}{dt} = \frac{\partial}{\partial t} + \boldsymbol{v}_\perp\cdot\nabla_\perp, \qquad \boldsymbol{v}_\perp = \left(\frac{R}{R_0}\right)^2\nabla\Phi\times\nabla\zeta, \tag{2.34}$$

respectively, and $\nabla_\perp \equiv \nabla - \nabla\zeta(\partial/\partial\zeta)$. The average curvature Ω is also given by (2.28). The equations (2.30), (2.31) and (2.32) correspond to the Ohm's law, the vorticity equation and the equation of state. This scheme has an advantage that it is easy to include the resistivity by taking nonzero η. They developed the RESORM code[26, 33] which solves the linearized version of these three field equations as an initial value problem. As the equations of (2.30)-(2.32) are nonlinear equation, the numerical scheme can be extended to the nonlinear version without any changes of the basic equations.

Both in the KSTEP and the RESORM codes, the Fourier expansion is employed in the poloidal and the toroidal direction. As the equilibrium quantities treated in the codes is averaged in the toroidal direction, the toroidal mode number of the perturbation can be specified in the stability calculation, while the poloidal mode coupling between the perturbation and the equilibrium quantities is incorporated.

2.1.4 Three-dimensional stability approach

As the development of the computer resources, the numerical codes analyzing the stability of the three-dimensional equilibria without any ordering or any averaging methods have been developed. The CAS3D and the TERPSICHORE codes are used in the stability analysis of the heliotron equilibria calculated by the VMEC code

The CAS3D[37, 44] code examines the ideal stability by solving an eigenvalue problem based on the energy principle. The Lagrangian for the displacement vector $\boldsymbol{\xi}$ is given by

$$L = \lambda W_K - W_P \tag{2.35}$$

with

$$W_K = \frac{1}{2}\int d^3r\rho_m|\boldsymbol{\xi}|^2 \tag{2.36}$$

$$W_P = \frac{1}{2}\int d^3r\left[|\boldsymbol{C}|^2 - A(\boldsymbol{\xi}\cdot\nabla s)^2 + \gamma P(\nabla\cdot\boldsymbol{\xi})^2\right] \tag{2.37}$$

$$\boldsymbol{C} = \nabla\times(\boldsymbol{\xi}\times\boldsymbol{B}) + \frac{\boldsymbol{J}\times\nabla s}{|\nabla s|^2}\boldsymbol{\xi}\cdot\nabla s \tag{2.38}$$

$$A = 2\frac{(\boldsymbol{J}\times\nabla s)\cdot(\boldsymbol{B}\cdot\nabla)\nabla s}{|\nabla s|^4} \tag{2.39}$$

In the descritization, the hybrid finite element is employed in the radial direction and the Fourier series are used in both the poloidal and toroidal angles. Since the three-dimensional equilibrium is used as it is, the mode coupling not only in the poloidal direction but also in the toroidal direction are taken into account. In this case, the perturbation space is divided into 'mode families'. As the Lagrangian has the quadratic form in the perturbation, only the combination of the Fourier modes of the perturbation with the toroidal mode numbers n_{p1} and n_{p2} satisfying the relation with an integer k,

$$n_{p1} \pm n_{p2} = kN_T, \tag{2.40}$$

gives the non-zero contribution to the Lagrangian, where N_T means the number of the field period of the equilibrium. Therefore, the Fourier modes of the perturbation is separated into $1+N_T/2$ mode families and the modes in the different families are independent.

In the previous version of the CAS3D code the incompressibility was assumed, however, the compressibility is appropriately treated in the recent version and the kinetic energy is treated so as to have a physical meaning[45].

The TERPSICHORE code[38, 46] also solves the eigenvalue problem based on the energy principle. Inspite that the TERPSICORE was developed independently with the CAS3D code, these codes are fairly similar in the formulation and the numerical scheme. The biggest difference between them would be the treatments of the vacuum region in the free boundary calculation. The Green's function is utilized in the CAS3D code, while the technique of the plasma with infinite resistivity is employed in the TERPSICHORE code.

3 Topics on MHD Studies in Heliotron Configuration

3.1 Three-dimensional Equilibrium Study

3.1.1 Boundary Condition in Equilibrium Study with the VMEC code

MHD equilibrium with the nested surfaces can be determined in principle with the boundary condition which gives the position and the shape of the outermost surface, the pressure profile and the profile of the net toroidal current or the rotational transform. Previously, in the heliotron configuration most of the equlibrium caluculations with the VMEC code[30, 31], were carried out under the fixed boundary condition because of the convenience of the calculation. However, it can be easily imagined the plasma column would move outward in the torus because of the diamagnetic effect as the beta value is increased. Hence, it is interesting to examine the difference of the MHD equilibrium between fixed boundary and free boundary conditions.

In the free-boundary calculation with the VMEC code, a constraint to determine the outermost surface is necessary. There is a stochastic region outside the outermost surface in the heliotron configuration. Ichiguchi et al.[47] considered that the position of right-hand edge of the horizontal cross section would be fixed at that in the vacuum configuration by the destruction of the flux surface due to the stochasticity of the field line when the plasma would move outward, that is, the stochastic region is assumed to play a role of a virtual limiter. Thus, they calculated the free-boundary LHD equilibria under the following two kinds of the constraint. One is the constraint that the plasma can be shifted outward in the torus freely and the other is that the additional vertical magnetic field is adjusted so that the position of the edge should be fixed with a feedback control.

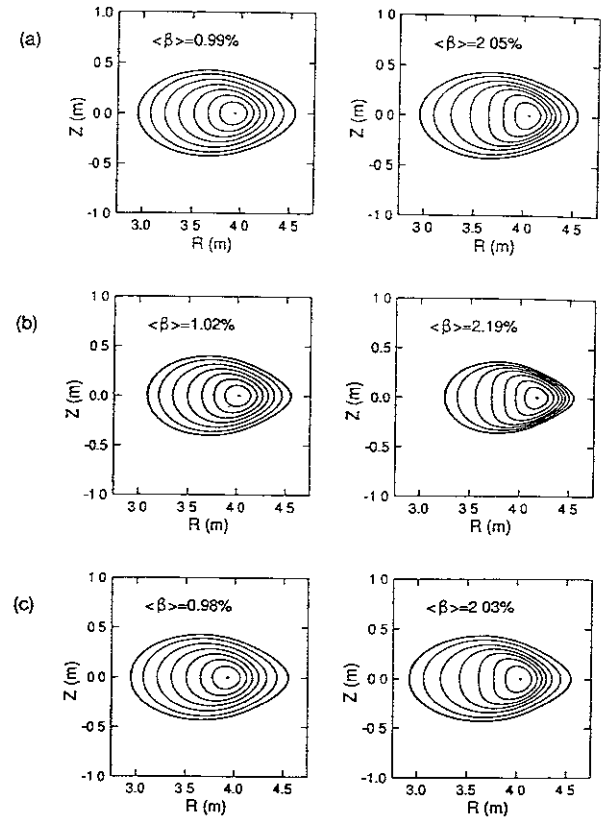

Fig.3.1.1 Flux surfaces for LHD equilibria in the plane of the horizontal ellipse for (a) fixed boundary, (b) free-shifted and (c) vertical-field control equilibria. [47]

Figure 3.1.1 shows the flux surfaces of the LHD free-bounaday equilibria with the pressure profile of $P(s) = P_0(1-s)^2$ under the currentless or the

no net toroidal current condition in the above constraints, which are compared with those under the fixed boundary condition. In the free-shifted equilibria, the volume decreases as the beta value increases, because the nested flux surfaces are destroyed at the outer edge by the stochastic region. On the other hand, the equilibria controlled with the vertical field have almost the same structure of the flux surface as the fixed boundary equilibria.

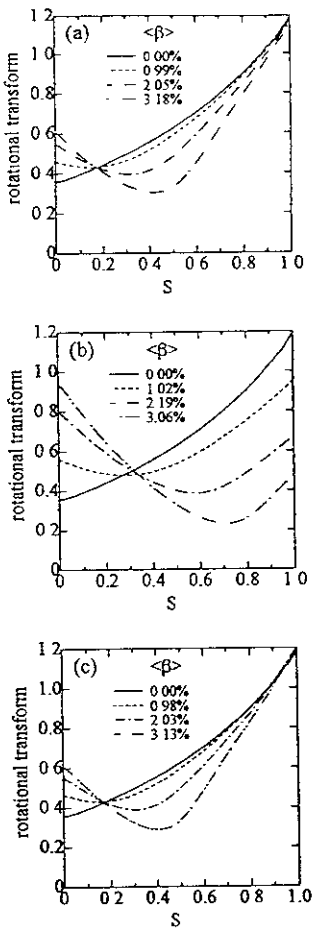

Fig.3.1.2 Rotational transform for (a) fixed, (b) free-shifted and (c) vertical-field control equilibria. [47]

Figure 3.1.2 shows the profiles of the rotational transform of the equilibria at several beta values for the fixed boundary, the free-shifted and the vertical-field control cases. As the beta value increases, the rotational transform in the fixed boundary equilibrium increases at the magnetic axis and decreases at the middle region so that the minimum value appears in the profile. Because of the change of the profile, the magnetic shear is enhanced in the peripheral region. This change in the profile is due to the deformation of the flux surfaces and is a general property of the currentless heliotron equlibrium. In the free-shifted case, this tendency is strongly enhanced and the value at the edge decreases owing to the reduction of the volume. In the vertical-field control case, the profile is very close to that in the fixed boundary case.

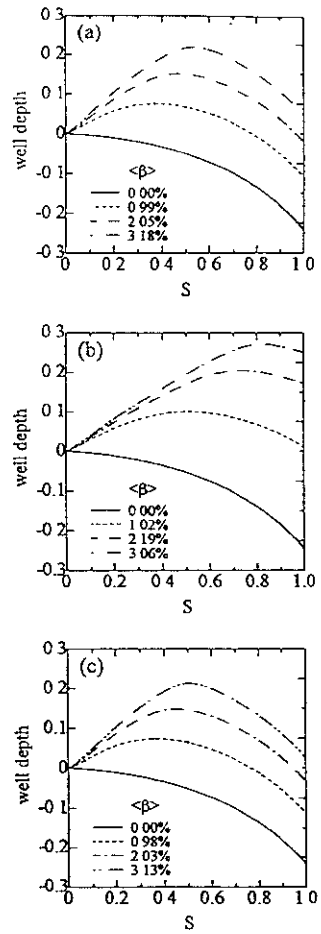

Fig.3.1.3 Magnetic well depth for (a) fixed, (b) free-shifted and (c) vertical-field control equilibria. [47]

Figure 3.1.3 shows the profile of the magnetic well depth defined by

$$\text{Well depth} \equiv \frac{V'(0) - V'(s)}{V'(0)}, \qquad (3.1)$$

where $V(s)$ denotes the volume bounded by the flux surface s. Therefore, in Fig.3.1.3, the region with the positive gradient of the curve corresponding to $V''(s) < 0$ shows the magnetic well region. In the

vacuum case, the magnetic hill is spread in the whole region, while the magnetic well is generated from the vicinity of the magnetic axis by the Shafranov shift as the beta value increases. The magnetic well region is wider in the free-shifted case than the fixed boundary case at the same beta value because the peripheral region with the magnetic hill is removed. The well depth in the vertical-field control case is also very similar to that in the fixed boundary case.

In the currentless equilibria, the pressure driven mode is the dominant mode, and the interchange mode is usually the most unstable in the heliotron configuration because there exists a magnetic hill region. It is very useful to evaluate the Mercier criterion[48, 49, 50] to examine the stability. The Mercier criterion is a stability criterion against the ideal interchange mode localized around the rational surface, which is given by

$$D_I = -(D_S + D_{J\cdot B} + D_W + D_{G.C.})/\iota'^2 < 0 \quad (3.2)$$

for the stability, where

$$D_S = \frac{\iota'^2}{4} \quad (3.3)$$

$$D_{J\cdot B} = \iota' \left\langle \frac{(I'\boldsymbol{B} - \boldsymbol{J})\cdot\boldsymbol{B}}{|\nabla\chi|^2} \right\rangle \quad (3.4)$$

$$D_W = P' \left(V'' - P' \left\langle \frac{1}{\boldsymbol{B}^2} \right\rangle \right) \left\langle \frac{\boldsymbol{B}^2}{|\nabla\chi|^2} \right\rangle \quad (3.5)$$

$$D_{G.C.} = \left\langle \frac{\boldsymbol{J}\cdot\boldsymbol{B}}{|\nabla\chi|^2} \right\rangle^2 - \left\langle \frac{\boldsymbol{B}^2}{|\nabla\chi|^2} \right\rangle \left\langle \frac{(\boldsymbol{J}\cdot\boldsymbol{B})^2}{\boldsymbol{B}^2|\nabla\chi|^2} \right\rangle . \quad (3.6)$$

Here ι and $2\pi\chi$ are the rotational transform and the toroidal magnetic flux, respectively. The prime means the derivative with respect to χ and the bracket is the flux average defined by

$$\langle f \rangle \equiv \frac{d}{d\chi} \int f dV. \quad (3.7)$$

The first term given by D_S is the magnetic shear term and always has a stabilizing effect. The term of D_W is the magnetic well term, including the V'' contribution. The last term of $D_{G.C.}$ is called the geodesic curvature term because the Pfirsch-Schlüter current which is the current parallel to the magnetic field is the solution of the magnetic differential equation

$$\boldsymbol{B}\cdot\nabla\sigma = \frac{2P'\boldsymbol{B}\times\nabla\chi\cdot\boldsymbol{\kappa}}{\boldsymbol{B}^2}, \quad (3.8)$$

where $\boldsymbol{\kappa}$ is the curvature of the field line given by $\boldsymbol{\kappa} = \boldsymbol{b}\cdot\nabla\boldsymbol{b}$ ($\boldsymbol{b} \equiv \boldsymbol{B}/B$) and σ is defined by $\sigma \equiv \boldsymbol{J}\cdot\boldsymbol{B}/B^2$. The second term $D_{J\cdot B}$ consists of the net toroidal current I and the parallel current, which can be recognized as a correction by the geodesic curvature to the magnetic well effect. Once an equilibrium is obtained, it is straightforward to calculate the Mercier criterion.

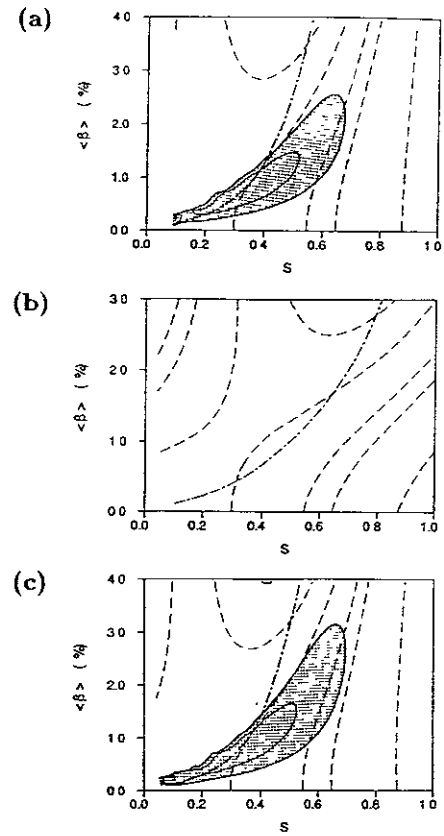

Fig.3.1.4 Mercier stability diagram for the (a) fixed, (b) free-shifted and (c) vertical-field control equilibria. Shaded regions in (a) and (c) show the region of Mercier instability. Solid lines in these regions are the contours of the level surface of D_I with the difference of $\Delta D_I = 0.1$. Dashed lines indicate the positions of rational surfaces corresponding to $\iota = 1$, 3/4, 2/3, 1/2 and 1/3 from right to left. The dot-dashed line marks the location of the transition between a magnetic well and a magnetic hill. [47]

Figure 3.1.4 shows the contours of the level surface of D_I in the Mercier unstable region with the positions of several rational surfaces in the fixed boundary, the free-shifted and the vertical-field control cases. In the fixed boundary equilibria, the region around the magnetic axis is stabilized by the magnetic well and the peripheral region is also stabi-

lized by the magnetic shear inspite of the magnetic hill. The middle region is slightly Mercier unstable as shown in Fig.3.1.4(a) because both stabilizing contribution is weak. As is discussed in Sec.3.2.1, it is considered that the absolute value of D_I is related to the growth rate of the corresponding global mode. Hence, the equilibrum is actually stable against the global interchange mode because the maximum of D_I is very small ($D_I \sim 0.1$). In the free-shifted case, the unstable region disappears completely. This is because the contribution of the magnetic well is strongly enhanced as shown in Fig.3.1.3(b). As are in the profiles of the rotational transform and the magnetic well depth, the behavior of D_I in the equilibria with the vertical-field control surprisingly agree with that of the fixed boundary equilibria. Hence, the equilibrium calculations under the fixed boundary condition are good approximations of the free boundary equilibria with the vertical-field control.

In the free boundary calculation, the magnetic field in the vacuum region outside the plasma is also caluculated. Such information can be useful in the experimental identification of the plasma column position.

3.1.2 Effects of horizontal plasma position

In heliotorns, the position of the plasma column or the outermost surface can be shifted horizontally in the vacuum configuration by changing the currents in the poloidal field coils to control the vertical magnetic field. The horizontal position control is the most basic freedom in the heliotoron configuration because the vertical field is inevitable to generate the magnetic surfaces. Generally speaking, when the plasma column is shifted inward or outward by the vertical field in the vacuum configuration, the magnetic axis is more shifted in the same direction than the outermost surfaces. In the case of the LHD, the position of the magnetic axis almost coincides with the position of the center of the outermost surface in the case of $\Delta_v = -15$cm, which is called the standard configuration. Here Δ_v denotes the position of the vacuum magnetic axis measured from the center of the helical windings. Hence, the magnetic axis is located outward from the center of the outermost surface for $\Delta_v > -15$cm while it is located inward for $\Delta_v < -15$cm. The relative relation of the positions between the magnetic axis and the center of the outermost surface definitely influences the magentic well. That is, the region of the good curvature of the field line extends if the magnetic axis is shifted outward.

The effects of the shift on the Mercier stability was investigated intensively in the fixed bounadry LHD equilibrium. Figure 3.1.5(b)[51] shows the Mercier

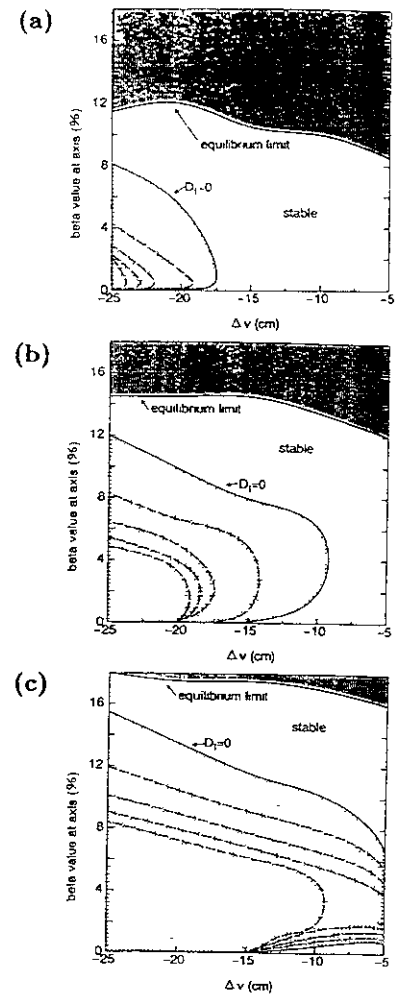

Fig.3.1.5 Mercier stability diagram in the LHD configuration for (a) $I = -50$kA (decreasing ι), (b) $I = 0$ (currentless) and (c) $I = +50$kA (increasing ι) with the equilibrium limits in the (β_0, Δ_v) plane. Dotted areas show unstable region. Dashed lines in these regions show the contours of the level surfaces of $D_I = 0.1$, 0.2, 0.3 and 0.4. [51]

unstable region with the level surfaces of D_I =0.1, 0.2, 0.3 and 0.4 in the $\beta_0 - \Delta_v$ space in the currentless equilibrium with the pressure $P = P_0(1-s)^2$. As is expected from the tendency in the magnetic well, the Mercier stability is improved as the magnetic axis is shifted outward. Hence, the configuration with the outward shifted axis is more favorable than that with inward shifted axis against the interchange mode. In the LHD case, however, the orbit of deeply trapped particle in the helical magnetic ripple becomes worse in the outward shifted case. Therefore, the configu-

ration with $\Delta_v = -15$cm which is marginally stable against the interchange mode ($D_I \leq 0.1$) is chosen as the standard configuration as a compromize between the MHD stability and the orbit loss of the particle. We also see the second stablity region at high beta against the Mercier mode. If an operation path to get into this region will be established, the stable operation against the interchange mode will be guaranteed.

3.1.3 Study of the magnetic island and the stochastic region with the HINT code

The HINT code[39] has been applied to heliotron plasma mainly to know how the vacuum nested surfaces generated by the external coils are destructed by the finite pressure. Figure 3.1.6[52] shows the

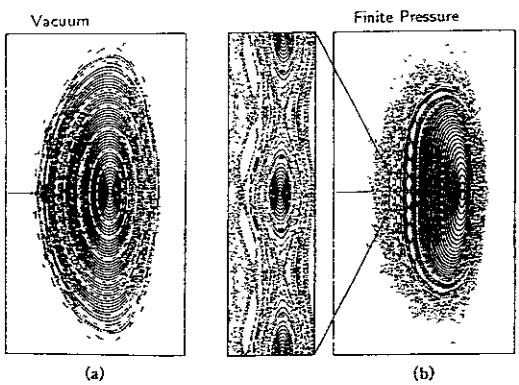

Fig.3.1.6 Poincaré plots of the magnetic field line for an LHD like configuration (a) for a vacuum field and (b) for a finite beta equilibrium. [52]

Poincaré plots of the magnetic field line of the vacuum field and the equilibrium at $\langle\beta\rangle = 3.7\%$ in the LHD like configuration. The magnetic surfaces are destroyed owing to the finite beta effect particularly in the peripheral region. The magnetic island chain can be also seen inside the plasma column.

The destruction of the magnetic surfaces results from the Pfirsch-Schlüter currents[53]. Under the existence of the assumption of the nested surfaces, the Pfirsch-Schlüter current which is the parallel component of the equilibrium current can be written as

$$\frac{\boldsymbol{J}\cdot\boldsymbol{B}}{B^2} = \frac{I'J - J'I}{I\Psi' + J\chi'} - \sum_{m\neq 0, n\neq 0} \frac{nI + mJ}{I\Psi' + J\chi'} \frac{P'\sqrt{g}_{mn}}{\chi'(m\iota - n)} \cos(m\theta - n\zeta) \quad (3.9)$$

where the Boozer coordinates[54] (s, θ, ζ) are employed and $\sqrt{g}_{mn}$ denotes a Fourier coefficient of the Jacobian. And $2\pi\chi$ and $2\pi\Psi$ are the toroidal and the poloidal magnetic fluxes, respectively, and $2\pi I$ and $2\pi J$ are the total toroidal current inside the flux tube and the poloidal total current outside the flux tube, respectively. The prime denotes the derivative with respect to s. From this equation, the current diverges at every rational surface of $\iota = n/m$ unless $\sqrt{g}_{mn} = 0$ or $P' = 0$. At the nested surfaces with $P' \neq 0$, such divergence is avoided by the condition $\sqrt{g}_{mn} = 0$. In the case of $\sqrt{g}_{mn} \neq 0$ at $\iota = n/m$ surface, $P' = 0$ should be satisfied so that the Pfirsch-Schlüter current should not be singular, which leads to the formation of the magnetic island or the stochastic region.

The theory to study the stability of the equilibrium including the magnetic island and the stochastic region against the interchange mode has not been established yet. However, the information of the change of the outermost surface due to the finite pressure is very useful in the determination of the outermost surface in the calculation of the VMEC code, of which result is widely used in the stability analysis.

3.2 Stability Boundary for Ideal Interchange mode

3.2.1 Relation between Mercier criterion and global modes

The main purpose in the stability analysis is to determine the stability boundary in specified parameters. Because the pressure driven mode is usually dominant in the heliotron plasmas, it is the most important issue to find out the critical beta value limited by the instabilities. Since the helical component of the vacuum magnetic field inherently generates the bad curvature of the field line, the ideal interchange mode has to be examined at first. In this point, to evaluate the Mercier criterion is very convenient as shown in the previous sections. As the Mercier criterion is a local stability criterion, it can indicate the equilibrium is unstable even in the case that the mode structure is extremely localized around the rational surface with infinitesimal mode width. Therefore, the Mercier limit may give too severe result in the evaluation of the stability and the global mode analysis should be needed to determine the actual beta limit. However, it has been shown that the Mercier criterion gives a good measure of the global stability and

we can roughly estimate the stability boundary due to the global mode by utilizing the criterion

In the one-dimensional case, the Mercier criterion is reduced to the Suydam criterion[55]. The criterion for the heliotron plasma is given by

$$\frac{1}{4}\left(\frac{d}{dr}\log\iota\right)^2 + \frac{4\pi}{B_\theta^2}\frac{dP}{dr}\frac{d\Omega}{dr} > 0, \qquad (3.10)$$

where the cylindrical coordinates (r, θ, z) are used and Ω is the averaged field line curvature given by eq.(2.28) under the cylindrical limit. Sugama and Wakatani[56] examined the relation between the critical beta value determined by the Suydam criterion and the low-n global interchange mode obtained numerically in the vicinity of the critical beta value. They showed that the low-n mode can be unstable only in the case $\beta > \beta_s$, where β_s is the beta limit given by the Suydam criterion and there exists a 'gap' between β_s and the critical beta value determined by the low-n mode as shown in Fig.3.2.1. In the one

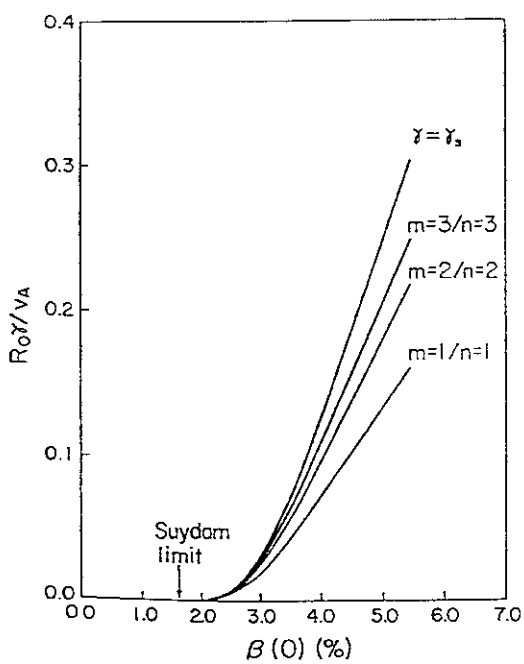

Fig.3.2.1 Growth rates of the $m = 1/n = 1$, $m = 2/n = 2$ and $m = 3/n = 3$ modes versus the central beta value $\beta(0)$. The upper curve shows the growth rate of the Suydam mode. [56]

dimensional case, the growth rate of the ideal interchange mode γ_s can be obtained analytically in the limit that the mode is quite localized in the vicinity of the resonant surface. This mode is called a Suydam mode. The behavior of the growth rate near β_s is approximately given by

$$\gamma_s \propto \exp\left(-\frac{const.}{\sqrt{\beta/\beta_s - 1}}\right), \qquad (3.11)$$

which shows that the critical beta value coincides to β_s. This equation shows that γ_s is quite small and flattened near the critical beta. Furthermore, the mode structure of the interchange mode extremely shrinks toward the resonant surface as the beta value approaches to the critical beta value from the value of the strongly unstable region. Because of above reasons, it is very difficult to obtain the ideal interchange mode just above β_s numerically. It accounts for the existence of the gap in the critical beta values determined by the Suydam criterion and the low-n global mode.

The similar relation is found between the Mercier criterion and the two dimensional stability calculation. Figure 3.2.2. shows the level surfaces of D_I

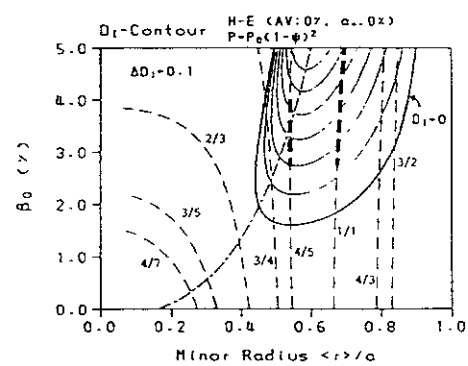

Fig.3.2.2 Contours of the Mercier parameter in the β_0 versus minor radius representation. The locations where the low-n unstable modes are found are indicated by the thick dashed lines. [57]

and the positions of the several rational surfaces[57] in a Heliotron E plasma. The gap can be seen also in this figure. It has been pointed out that the unstable mode can be usually obtained in the region with $D_I \geq 0.2$. Fu et al.[46] also obtained a similar relation by using the three-dimensional stability code TERPSICHORE[38]. The low-n mode would be marginally unstable with a small growth rate in the region $0 < D_I \leq 0.2$. However, such a marginally

unstable mode can be easily stabilized by some kinetic effects such as the finite Larmor radius effect. Therefore, we should treat the Mercier criterion as a measure of the stability against the ideal interchange mode, which indicates that the global mode may be unstable for $D_I > 0.2$ rather than $D_I > 0$.

3.2.2 Effects of pressure flattening

Since the interchange mode is driven by the pressure gradient, it can be stabilized by flattening the pressure profile around the resonant surface. It was shown by Ichiguchi et al.[58], how effectively the mode is stabilized by the pressure flattening in the LHD configuration with inward-shifted vacuum magnetic axis. Figure 3.2.3 shows the profile of the

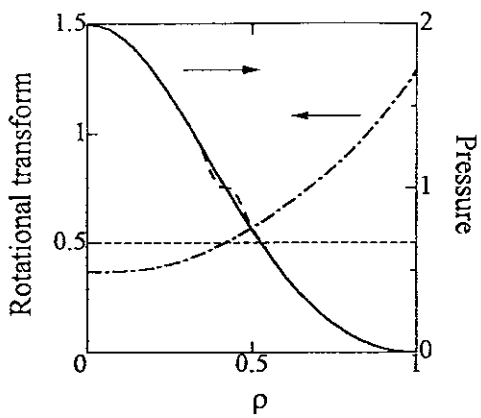

Fig.3.2.3 Profiles of the rotational transform (dashed-dotted line) and the pressure at $\beta(0) = 2\%$ in the inward-shifted LHD configuration. Solid and dashed lines show the smooth and the flattened ($w = 0.035$) pressure profiles, respectively. [58]

rotational transform of a currentless equilibrium at $\beta_0 = 2\%$, where β_0 denotes the beta value at the magnetic axis, with the smooth pressure profile P_S given by

$$P_s(\rho) = P_0(1-\rho^2)^2, \quad (\rho = \sqrt{s}), \qquad (3.12)$$

which is shown by the solid line. In this case, there exists the rational surface with $\iota = 1/2$ in the plasma column. The stability calculation with the RESORM code gives an unstable $n = 1$ ideal mode. Figure 3.2.4 shows the mode structure of the stream function. The dominant component is $m = 2$ which is

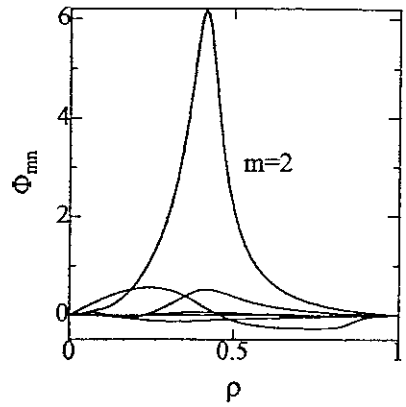

Fig.3.2.4 Fourier components of the stream function of the $n = 1$ ideal mode at $\beta(0) = 2\%$ with the smooth pressure profile in the inward-shifted LHD configuration. [58]

resonant at the surface with $\iota = 1/2$ and shows a typical interchange type structure. The half-width of the component is 0.14 in ρ.

The effects of the pressure flattening is considered by assuming the profile of

$$P = P_s + \lambda(\rho - \rho_s)\exp\left[-\frac{1}{2}\left(\frac{\rho-\rho_s}{w}\right)^2\right]. \qquad (3.13)$$

Here w is the measure of the width of the flattened region, and λ is determined so as to satisfy $dP/d\rho = 0$ at a specified position, $\rho = \rho_s$. In this case, $\rho_s = \rho|_{\iota=1/2}$ is chosen to see the stabilizing effects of the interchange mode. The flattened pressure profile for $w = 0.035$ is also plotted in Fig.3.2.3. The difference between the smooth and the flattened profiles is very small in this value of w. The size of the flattened width is too small to influence the profile of the rotational transform. However, this small flattened region plays a significant role in the stability. Figure 3.2.5 shows the dependence of the growth rates of the interchange mode on the width of the flattened region. The mode is effectively stabilized by enlarging the width, and is completely stabilized by the pressure flattening with $w = 0.037$ at $\beta_0 = 2\%$ which is about a quarter of the half-width of the mode for the smooth pressure profile. Similar stabilization is also obtained at $\beta_0 = 1$ and 3% as shown in Fig.3.2.5. Thus, the interchange mode can be stabilized by flattening the pressure at the resonant surface with much

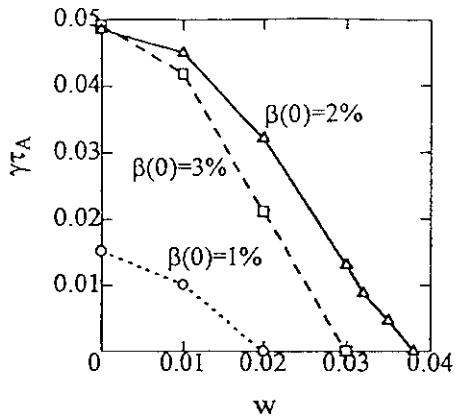

Fig.3.2.5 Growth rate of the n=1 ideal mode in the inward-shifted LHD configuration at $\beta(0)$ =1, 2 and 3% versus the width of the pressure flattened region. [58]

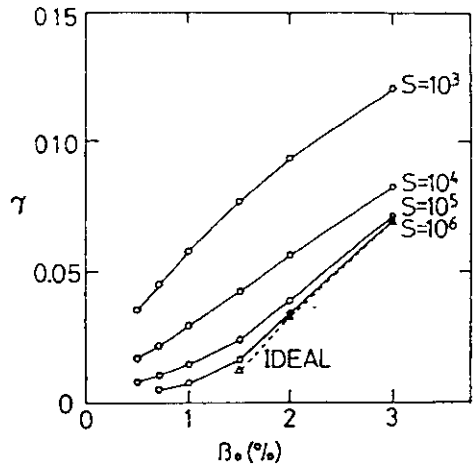

Fig.3.3.1 Growth rates of the n=1 resistive interchange modes versus β_0 for $S = 10^3$, 10^4, 10^5 and 10^6. The growth rates at $S = \infty$ (ideal case) are shown for comparison (dotted line). [26]

narrower width of the flattened region than the half width of the mode.

One of the possible ways to control of such pressure flattening is utilizing the magnetic island formation. In the LHD, the local island divertor coils are provided so as to generate a magnetic island at the edge of the plasma region[59]. The islands can be generated also inside the plasma column by controlling the currents in the coils. On the other hand, Carreras et al.[60] show the possibility that the nonlinear saturation of the resistive interchange mode flattens the pressure profile at rational surfaces automatically.

3.3 Resistive Interchange mode

3.3.1 Properties of the resistive interchange mode

There always exists finite resistivity in the plasma. Hence it is important to study the stability against the resistive modes. In this case, it is useful to utilize the technique based on the reduced MHD equations because including the resistivity is very easy.

Figure 3.3.1 shows the growth rates of the $n = 1$ instability for several S in the Heliotron DR current-less equilibrium calculated with the RESORM code. Here S is the magnetic Reynolds number which is defined by

$$S \equiv \frac{\tau_R}{\tau_A} \tag{3.14}$$

with the resistive diffusion time $\tau_R = a^2/\eta$ and the poloidal Alfvén time $\tau_A = R_0\sqrt{\rho_m}/B_0$ where a and ρ_m denote the average minor radius and the mass density. The mode structure corresponding to each growth rate of this figure shows the shape of the typical interchange mode.

In the ideal limit, the beta value at the magnetic axis limited by the $n = 1$ interchange mode and the critical beta value is $\beta_{0c} = 1.2\%$ as shown in Fig.3.3.1. On the other hand, it is obtained that the Mercier limit is $\beta_0 = 0.7\%$, and therefore, the gap between the critical beta values discussed in Sec.3.2.1 can be seen. For the finite S values, the resistive interchange modes are obtained. In the region with $\beta_0 \geq \beta_{0c}$, the growth rates of the resistive interchange mode are larger than those of the ideal mode. This is because the 'frozen-in' condition of the magnetic flux is relaxed by the finite resistivity, and therefore, the freedom of the perturbation is extended. Furthermore, the resistive interchange mode can also be unstable in the region of $0 < \beta_0 < \beta_{0c}$. This result can be understood from the fact that the growth rate obtained in the cylindrical limit scales as

$$\gamma \propto \left(\frac{m^2\beta_0^2}{S}\right)^{1/3} \tag{3.15}$$

in the bad curvature region[62]. Because there always exists a magnetic hill region in the vacuum heliotron configuration, the resistive interchange mode can be also unstable at a small beta value.

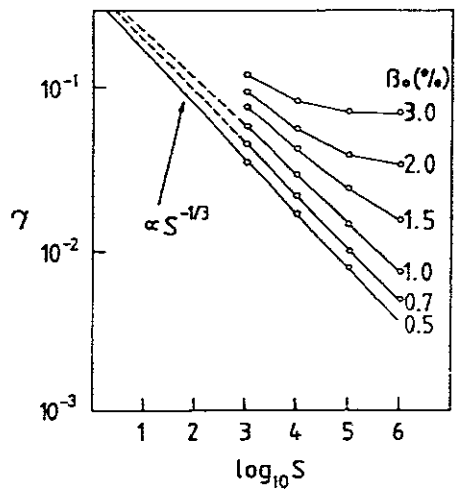

Fig.3.3.2 Dependence of the growth rate of the n=1 mode on the magnetic Reynolds number S for various β_0. [26]

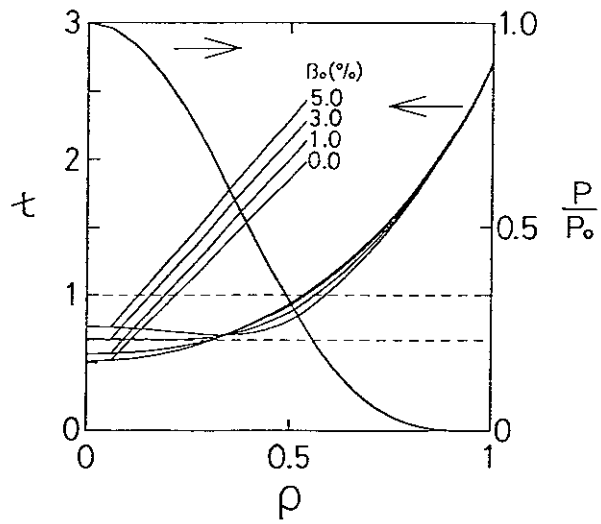

Fig.3.3.3 Profiles of the rotational transform at several beta values and the normalized pressure, $P/P_0 = (1-\rho^2)^4$, where $\rho = \sqrt{\Psi_{eq}}$, in Heliotron E currentless equilibria. [33]

Figure 3.3.2 shows the S dependence of the $n = 1$ mode at several beta values. In the case of $\beta_0 = 0.5\%$, where the ideal mode is completely stable, the growth rates are proportional to $S^{-1/3}$. This means the mode is consistent with eq.(3.15) in the ideal stable region. As the beta value increases, the deviation from the $S^{-1/3}$ dependence becomes large. This is due to the influence of the ideal mode on the growth rates of the resistive mode. The deviation appears even at $\beta_0 = 0.7\%$ and 1.0%, where there is no unstable global ideal mode but $D_I > 0$. As discussed in Sec.3.2.1, these beta values correspond to the marginal unstable region against the ideal interchange mode or the 'gap ' region. Therefore, the properties of the low-n resistive mode are affected by the ideal instability in the Mercier unstable region even if it is difficult to obtain a global ideal interchange mode by a numerical calculation.

3.3.2 Non-resonant modes

The RESORM code numerically found a new type of non-resonant or near-resonant resistive pressure driven mode localized near the magnetic axis in heliotron configurations[33]. This mode appears in the case with a pressure profile peaked at the magnetic axis. Figure 3.3.3 shows the profiles of the rotational transform in the Heliotron E equilibria with highly peaked pressure profile,

$$P = P_0(1-\rho^2)^4. \tag{3.16}$$

Here, ρ denotes the square root of the normalized poloidal magnetic flux. The magnetic shear in the region around the magnetic axis is easily reduced by the finite beta effect. In the case with high resistivity of $S < 10^3$, a mode of which the stream function has a ballooning-like structure as shown in Fig.3.3.4(a). Each Fourier component of the stream functions is not resonant at the rational surface, but localized around the magnetic axis. In this region, the magnetic shear is very weak and the pressure gradient is substantial. Therefore, the mode which is not resonant at the rational surface can be unstable in the vicinity of the magnetic axis.

It is also obtained that the property of the non-resonant structure still remains in the increase of the beta value. Following the change of the rotational transform profile at finite beta values, however, the dominant poloidal Fourier component of the mode changes so as to make the parallel wave number small (not zero). As S increases, the radial mode structure becomes narrower and the peak position approaches the magnetic axis, as shown in Fig.3.3.4(b). Figure 3.3.5 shows the growth rate of the mode as the function of S. The numerically obtained growth rate is proportional to $S^{-1/3}$. In the increase of S, a tran-

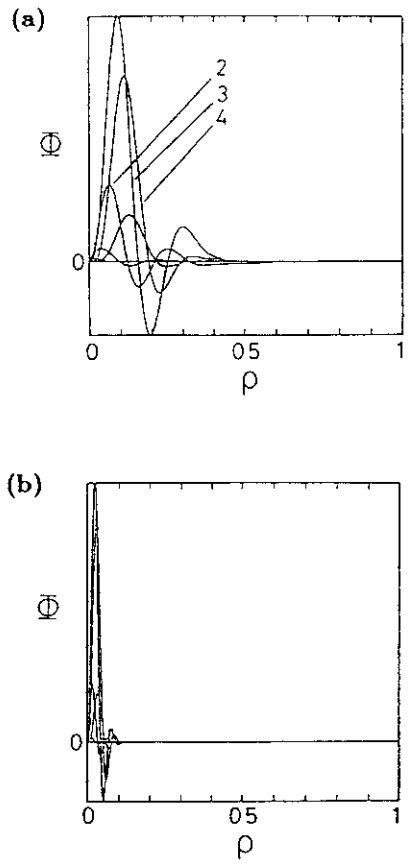

Fig.3.3.4 Stream function Φ with n=2 at $\beta_0 = 1\%$ in the equilibrium of Fig.3.3.3 for (a) $S = 10^3$ and (b) $S = 10^5$. The numbers denote poloidal mode numbers. [33]

sition to an unstable resistive interchange mode localized at a resonant surface occurs at a critical S value.

In order to understand the properties of the non-resonant mode, the dispersion relation was also derived analytically in the electrostatic approximation in the cylindrical geometry. In the electrostatic approximation, the three-field equations are reduced to an ordinary differential equation given by

$$\gamma \nabla_\perp^2 \Phi_{mn} = S(n - m\iota)^2 \Phi_{mn} - \frac{D_s}{\gamma} \frac{m^2}{r^2} \Phi_{mn} \quad (3.17)$$

for a specified Fourier component of the stream function, Φ_{mn}, in the cylindrical coordinates (r, θ, ζ). Here D_s is the driving contribution by the pressure

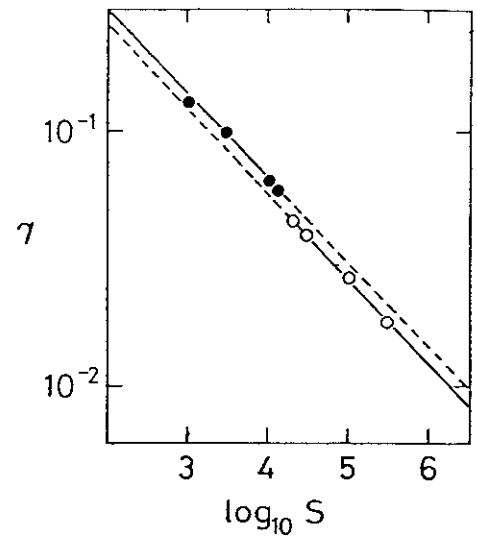

Fig.3.3.5 Dependence of the growth rate on the magnetic Reynolds number of the mode corresponding to Fig.3.3.4. The closed and the open circles correspond to the non-resonant mode and the resistive interchange mode, respectively. For all lines, $\gamma \propto S^{-1/3}$ is assumed. γ is normalized to the poloidal Alfvén time. [33]

gradient defined as

$$D_s \equiv -\frac{\beta_0}{2\epsilon^2} P' \Omega', \quad (3.18)$$

where ϵ denotes the inverse aspect ratio and the prime means the derivative with respect to r. In this cylindrical configuration, the averaged magnetic curvature is attributed to only the helical component in eq.(2.28), which can be written as

$$\Omega' = \epsilon^2 \frac{N}{l} \frac{1}{r^2} \frac{d}{dr}(r^4 \iota) \quad (3.19)$$

where l and N are the pole number and the number of the field period of the helical windings.

Here, it is assumed that the mode is localized around a certain point, $r = r_p$, the magnetic shear is very weak so that $\iota'(r_p) \simeq 0$, and the pressure gradient is constant around $r = r_p$. Then, D_s becomes a linear function of r and can be written as $D_s = C_p r$, and the parallel wave number, $k_\parallel = n - m\iota$, becomes almost constant. By setting

$$r_p = \frac{1}{2} \left(\frac{C_p m^2}{S k_\parallel^2} \right)^2, \quad (3.20)$$

and transforming $y = \sqrt{r}\Phi_{mn}$ and $x = r - r_p$, eq.(3.17) can be reduced to a Weber type equation which has a dispersion relation given by

$$\gamma^3 = \frac{C_p^2 m^4}{(2m+1)^2 S k_{\|}^2} \tag{3.21}$$

for the largest growth rate. The corresponding eigenfunction is the zeroth parabolic cylindrical function expressed as

$$\Phi_{mn} = \frac{1}{\sqrt{r}} \exp\left[-\frac{1}{H}(r - r_p)^2\right] \tag{3.22}$$

$$r_p = \frac{1}{2}\left[\frac{(2m+1)^2 C_p m^2}{S^2 k_{\|}^4}\right]^{1/3}, \tag{3.23}$$

where H is a function of C_p, S and $k_{\|}$. This analytic eigenfunction explains well the tendency that the mode structure shrinks and approaches the magnetic axis because $H \propto S^{-2/3}$ and $r_p \propto S^{-2/3}$. Besides, eq.(3.21) accounts for the dependence of $\gamma \propto S^{-1/3}$ and the fact that the smaller $k_{\|}$ gives the larger γ, which are also shown in the numerical results.

The reason why the ballooning like structure is obtained numerically is because the toroidicity component is dominant in Ω (the first term of eq.(2.28)) in the vicinity of the magnetic axis rather than eq.(3.19). The transition can be explained by the following consideration. The region of the free energy of the non-resonant mode is more reduced than that of the resistive interchange mode as S increases. Thus, when the free energy becomes smaller than that of the resistive interchange mode at a critical S value, the transition occurs and the resistive interchange mode becomes dominant in the growth rate beyond the S value.

3.4 Effects of Net Toroidal Current

3.4.1 Effects of the peaked current density on the interchange mode

The heliotron configuration has an advantage that there exists an equilibrium without any net toroidal current. In practice, however, the net toroidal current can flow in the plasma column due to some transport process, such as the bootstrap current and the beam current. Besides, the Ohmic current can be driven by providing the inductive coils like tokamaks. Therefore, it is very important to study the effects of the net toroidal current on the MHD properties in heliotron plasmas. The effects of the net toroidal current on the Mercier stability in the LHD configuration were studied intensively with a given current density by Ichiguchi et al.[51]

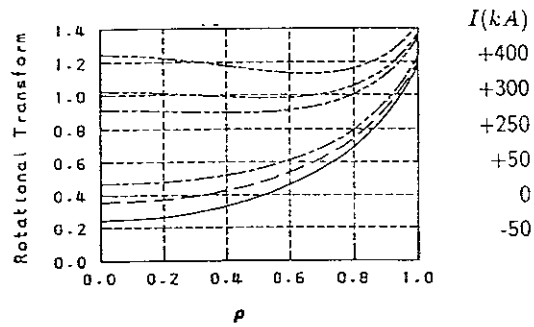

Fig.3.4.1 Profiles of the rotational transform in the LHD equilibria with $B_0 = 3$T at $\beta_0 = 0\%$ carrying several net toroidal currents.

The net toroidal current changes the profile of the rotational transform through the direct effect on the poloidal magnetic field. Figure 3.4.1 shows the profile of the rotational transform for several net toroidal current in the LHD standard configuration at $\beta_0 = 0\%$, where I denotes the total toroidal current and B_0 is assumed to be 3T. In this figure, the net toroidal current density J is assumed to be

$$J = J_0(1 - s)^2. \tag{3.24}$$

As is shown in this figure, the positive I corresponds to the increase of the rotational transform and the negative one to the decrease.

The effects of this net toroidal current on the Mercier criterion is summarized in the diagrams of Fig.3.1.5 (a) and (c). As is shown in these figures, the Mercier stability is improved by the current decreasing the rotational transform and is deteriorated by the one increasing the rotaional transform. The mechanism of the contribution to the Mercier stability can be understood by considering the magnetic well. In the limit of large aspect ratio and low beta, the Shafranov shift of the magnetic axis is nearly proportional to ι_0^{-2}, where ι_0 denotes the rotational transform at the magnetic axis[61]. Figure 3.4.2 shows that this tendency is seen in the LHD plasmas carrying the net toroidal current. That is, the reduction of the rotational transform for $I = -50$kA permits a large Shafranov shift in the finite beta equilibrium,

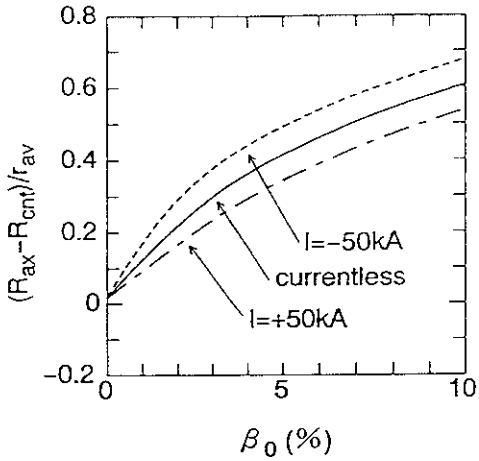

Fig.3.4.2 Shafranov shift of the LHD equilibria in standard configuration ($\Delta_v = -15$cm). The dotted, solid and the dot-dashed lines show the cases of $I = -50$kA (decreasing ι), $I = 0$kA (currentless) and $I = +50$kA (increasing ι), respectively. [51]

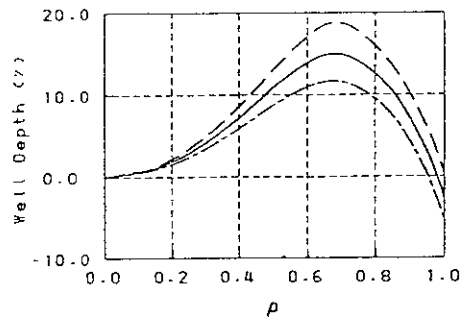

Fig.3.4.3 Magnetic well depth of the LHD equilibria in standard configuration ($\Delta_v = -15$cm). The dashed, solid and the dot-dashed lines show the cases of $I = -50$kA (decreasing ι), $I = 0$kA (currentless) and $I = +50$kA (increasing ι), respectively. [51]

which is defined by the difference between the major radius of the magnetic axis, R_{ax}, and the major radius of the outermost surface, R_{cnt}, normalized by the average radius of the outermost surface, r_{av}, here. The large Shafranov shit deepens the magnetic well. Figure 3.4.3 shows the well depth at $\beta_0 = 6\%$. The width of the well region is almost independent of the net toroidal current. However, the absolute value of V'' is increased by the current of $I = -50$kA. Thus, the enhancement of the magnetic well brings the stability contribution against the Mercier mode in this case. On the contrary, the suppression of the well formation makes the equilibrium unstable in the case of $I = +50$kA.

It is noted that the tendency that the outward shift of the magnetic axis in Δ_v stabilizes the Mercier mode and the inward shift destabilizes the mode is common in each net toroidal current case as shown in Fig.3.1.5. This means that the effect of the net toroidal current on the Mercier criterion is almost independently superposed on the effect of the magnetic axis shift due to the vertical field.

In Fig.3.1.5, the equilibrium limit is also drawn in each case of I. The large Shafranov shift pushes the magnetic surfaces toward the outward of the torus. As the beta value increases, the contour of the magnetic flux labeled by s becomes dense in the outward region of the plasma column and the pressure gradient becomes locally steep in such region. When the pressure gradient becomes too steep to balance the magnetic force, the equilibrium beta limit appears. In the $I = -50$kA case, the large Shafranov shift is favorable in the Mercier stability; however, it brings lower equilibrium beta limit.

3.4.2 Formulation of the bootstrap current in three-dimensional configuration

Among the various net toroidal currents in the heliotron configuration, the bootstrap current is especially important, because it is generated without any external current driving source. According to the neoclassical transport theory, the bootstrap current results from the balance of the viscosity between the trapped particles and the passing particles and the collision with the particles of other species. Here we review the formulation of bootstrap current in three-dimensional configuration briefly[63, 64, 65, 66].

The first order of the moment equations in the neoclassical ordering gives the balance equations for the momentum and the heat flux. The balance equations which are flux-averaged and parallel to the magnetic field line are written as[65]

$$\begin{pmatrix} \langle \boldsymbol{B}\cdot\nabla\cdot\boldsymbol{\Pi}_a\rangle \\ - \langle \boldsymbol{B}\cdot\nabla\cdot\boldsymbol{\Theta}_a\rangle \end{pmatrix} = \begin{pmatrix} \langle \boldsymbol{B}\cdot\boldsymbol{F}_{a1}\rangle \\ - \langle \boldsymbol{B}\cdot\boldsymbol{F}_{a2}\rangle \end{pmatrix}. \quad (3.25)$$

Here, the effects of fast ion, charge exchange and inductive electric field are neglected for simplicity. $\boldsymbol{\Pi}$,

Θ, $\boldsymbol{F}_1$ and $\boldsymbol{F}_2$ denote the particle viscosity, the heat viscosity, the particle friction and the heat friction, respectively. Subscript a means the species of the particle and the bracket represents the flux average. The parallel friction can be expressed as[67]

$$\begin{pmatrix} \langle \boldsymbol{B}\cdot\boldsymbol{F}_{a1}\rangle \\ -\ \langle \boldsymbol{B}\cdot\boldsymbol{F}_{a2}\rangle \end{pmatrix} = \sum_b \begin{pmatrix} l_{11}^{ab} & l_{12}^{ab} \\ l_{21}^{ab} & l_{22}^{ab} \end{pmatrix} \begin{pmatrix} \langle \boldsymbol{B}\cdot\boldsymbol{u}_b\rangle \\ -\dfrac{2}{5P_a} \quad \langle \boldsymbol{B}\cdot\boldsymbol{q}_b\rangle \end{pmatrix}, \tag{3.26}$$

where $\boldsymbol{u}$ and $\boldsymbol{q}$ are the particle flow and the heat flow, respectively, and l_{ij}'s are the friction coefficients.

The parallel viscosity is given by evaluating the solution of the first-order drift kinetic equation for the gyro-averaged distribution function. This solution directly depends on the orbits of the particles which reflects the influence of the magnetic configuration and the collisionality of the species. The first-order drift kinetic equation can be analytically solved in the limits of the $1/\nu$, the plateau and the Pfirsch-Schlüter collisionality regimes. Hence, the solution gives only the asymptotic expressions of the parallel viscosity in each collisionality regime, which can be summarized as[66]

$$\begin{pmatrix} \langle \boldsymbol{B}\cdot\nabla\cdot\boldsymbol{\Pi}_a\rangle \\ -\ \langle \boldsymbol{B}\cdot\nabla\cdot\boldsymbol{\Theta}_a\rangle \end{pmatrix} = \begin{pmatrix} \mu_{a1} & \mu_{a2} \\ \mu_{a2} & \mu_{a3} \end{pmatrix} \begin{pmatrix} \langle \boldsymbol{u}_a\cdot\nabla\theta_a^*\rangle \\ -\dfrac{2}{5P_a} \quad \langle \boldsymbol{q}_a\cdot\nabla\theta_a^*\rangle \end{pmatrix} \tag{3.27}$$

with

$$\theta_a^* = (I + G_b)\theta + (J - \iota G_b)\zeta, \tag{3.28}$$

where μ_{ai}'s are the viscosity coefficients. Here the Boozer coordinates (χ, θ, ζ) are used. The main role of the parallel viscosities are to transfer the momentum between the particles of the same species through damping the flow and the heat flux in such a direction that the magnitude of the magnetic field varies. Equation (3.27) shows that the direction of the viscosity damping is determined by θ_a^*. This angle is characterized by G_b which is called the geometrical factor. In tokamak case, for example, the geometrical factor is given by $G_b^{tok} = J/\iota$, which implies that the damping direction is the poloidal direction. On the contrary, in the three-dimensional configuration, G_b varies depending on the magnetic geometry and the collisionality regime of the particles, and therefore, the damping direction as well.

From the lowest order of the moment equations, the flow and the heat flux perpendicular to $\boldsymbol{B}$ are obtained,

$$\boldsymbol{u}_{\perp a} = A_{1a}\frac{\boldsymbol{B}\times\nabla\chi}{B^2} \tag{3.29}$$

and

$$\boldsymbol{q}_{\perp a} = \frac{5P_a}{2}A_{2a}\frac{\boldsymbol{B}\times\nabla\chi}{B^2}. \tag{3.30}$$

Here A_1 and A_2 are the thermodynamic forces given by

$$A_{1a} = \frac{1}{e_a n_a}\frac{dP_a}{d\chi} + \frac{d\Phi_\chi}{d\chi} \tag{3.31}$$

and

$$A_{2a} = \frac{1}{e_a}\frac{dT_a}{d\chi}, \tag{3.32}$$

where e, n, T and Φ_χ denote the charge of the particle, the density, the temperature and the radial electric potential, respectively. Utilizing the expressions of (3.29) and (3.30), the left hand side of eq.(3.27) is given by

$$\begin{pmatrix} \langle \boldsymbol{u}_a\cdot\nabla\theta_a^*\rangle \\ \langle \boldsymbol{q}_a\cdot\nabla\theta_a^*\rangle \end{pmatrix} = \begin{pmatrix} \langle \boldsymbol{B}\cdot\boldsymbol{u}\rangle + \quad G_{ba}A_{1a} \\ \langle \boldsymbol{B}\cdot\boldsymbol{q}\rangle + \dfrac{2}{5P_a}G_{ba}A_{2a} \end{pmatrix}. \tag{3.33}$$

By solving the balance equations (3.25) for the parallel momentum and heat flux with (3.26), (3.27) and (3.33), the bootstrap current can be evaluated by

$$\langle \boldsymbol{B}\cdot\boldsymbol{J}_b\rangle = \sum_a e_a n_a \langle \boldsymbol{B}\cdot\boldsymbol{u}_a\rangle. \tag{3.34}$$

Here, we assume that the plasma is composed of electrons and protons, and the temperature and the density of the electrons equals to those of the protons, respectively, and the radial electric field is neglected. In this case, the asymptotic expression of the total bootstrap current, I_b, in each collisionality regime can be written as

$$I_b = 2\pi\int d\chi \frac{\langle \boldsymbol{J}_b\cdot\boldsymbol{B}\rangle}{\langle \boldsymbol{B}^2\rangle}, \tag{3.35}$$

$$\langle \boldsymbol{J}_b\cdot\boldsymbol{B}\rangle = -G_b\left(L_1\frac{dP}{d\chi} + L_2 n\frac{dT}{d\chi}\right), \tag{3.36}$$

where L_1 and L_2 are the transport coefficients composed of the collision and the viscosity coefficients. As is seen from eq.(3.36), the change of G_b is important in the evaluation of the bootstrap current in heliotron configurations because it can change the direction of the current through the change of the flow damping.

In the limit of the $1/\nu$ regime, the geometrical factor, $G_b^{1/\nu}$, is given by following equations[65],

$$G_b^{1/\nu} = \frac{1}{f_t}\left\{\langle g_2\rangle - \frac{3}{4}\frac{\langle B^2\rangle}{B_{max}^2}\int_0^1 \frac{\langle g_4\rangle}{\langle g_1\rangle}\lambda d\lambda\right\} \tag{3.37}$$

and

$$g_1 = \sqrt{1-\lambda\frac{B}{B_{max}}}, \tag{3.38}$$

where f_t is the fraction of the trapped particles given by

$$f_t = 1 - \frac{3}{4}\frac{\langle B^2\rangle}{B_{max}^2}\int_0^1 \frac{1}{\langle g_1\rangle}\lambda d\lambda, \tag{3.39}$$

and g_2 and g_4 satisfy the magnetic differential equations of

$$\boldsymbol{B}\cdot\nabla\left(\frac{g_2}{B^2}\right) = \boldsymbol{B}\times\nabla\chi\cdot\nabla\left(\frac{1}{B^2}\right) \qquad g_2(B_{max}) = 0 \tag{3.40}$$

and

$$\boldsymbol{B}\cdot\nabla\left(\frac{g_4}{g_1}\right) = \boldsymbol{B}\times\nabla\chi\cdot\nabla\left(\frac{1}{g_1}\right), \qquad g_4(B_{max}) = 0, \tag{3.41}$$

respectively. The geometrical factor in the limit of the plateau regime, G_b^{pl}, is given by[68]

$$G_b^{pl} = \langle g_2\rangle - \frac{\sqrt{\pi}}{2}(J+\iota I)\lambda_{pl}h_1 \tag{3.42}$$

$$h_1 = \left\langle n_B \sum_{m\neq 0 \ or \ n\neq 0} \frac{(\boldsymbol{n}\cdot\nabla g_2/(2B^2))_{mn}e^{i(m\theta+n\zeta)}}{|m\iota+n|}\right\rangle \tag{3.43}$$

and

$$\lambda_{pl} = \frac{2\langle B^2\rangle}{\sqrt{\pi}(J+\iota I)h_2} \tag{3.44}$$

$$h_2 = \left\langle n_B \sum_{m\neq 0 \ or \ n\neq 0} \frac{1}{|m\iota+n|}\left(\frac{n_B}{B}\right)_{mn} e^{i(m\theta+n\zeta)}\right\rangle, \tag{3.45}$$

where

$$n_B = \boldsymbol{n}\cdot\nabla B, \tag{3.46}$$

and

$$A_{mn} = \frac{1}{(2\pi)^2}\int_0^{2\pi} d\theta \int_0^{2\pi} d\zeta A \exp i(m\theta+n\zeta). \tag{3.47}$$

Here $\boldsymbol{n}$ is the unit vector along the magnetic field and $2\pi I$ is the total toroidal current inside the flux surface. Since the plasma collisionality in the recent heliotron plasmas is usually between the $1/\nu$ and the plateau regimes, the factor in the Pfirsch-Schlüter regime is not discussed here.

In order to obtain the bootstrap current of the plasma with any collisionality between above two limits, a connection formula given by Watanabe et al.[68] is utilized for the products of G_b and L_j in (3.36) for j =1 and 2. In the connection formula, the collision frequency normalized by the bounce frequency, ν_*, is used as the parameter of the collisionality, which is defined by[68]

$$\nu_* = \frac{4}{3\sqrt{\pi}}\frac{f_t}{1-f_t}\frac{\lambda_{pl}}{\lambda}, \tag{3.48}$$

where λ denotes the mean free path of the particle. Although ν_* depends on the species of the particle in general, the ions and the electrons have the same value here because it is assumed that they have the same density and temperature. The limits of $\nu_* << 1$ and $\nu_* >> 1$ correspond to the $1/\nu$ and the plateau collisionality regimes, respectively. The connection formula is derived so that the the products of G_b and L_j in each limit should be given by the asymptotic expressions. Therefore, the expression of the products between the two limits has the form of

$$L_jG_b = \tilde{M}_j^{1/\nu}(\nu_*)G_b^{1/\nu} + \tilde{M}_j^{pl}(\nu_*)G_b^{pl}. \tag{3.49}$$

Here $\tilde{M}_j$ consists of the asymptotic values of L_j and the weight function depending on ν_*. In the limit of $\nu_* << 1$, $\tilde{M}_j^{pl}$ approaches to zero and $\tilde{M}_j^{1/\nu}$ gives the asymptotic value of L_j in the $1/\nu$ regime. In the limit of $\nu_* >> 1$, $\tilde{M}_j^{1/\nu}$ approaches to zero and $\tilde{M}_j^{pl}$ gives the asymptotic value of L_j in the plateau regime. The exact expression of the connection formula is given in Ref.[68].

3.4.3 Collisionality dependence of the bootstrap current

As is mentioned in the previous section, in a three-dimensional configuration the parallel viscosity has different form in the limit of each collisionality. Hence, the bootstrap current in the heliotron configuration strongly depends on the collisionality of the plasma.

In order to calculate the geometrical factor, the information of the equilibrium magnetic field is necessary. On the other hand, the net toroidal current including the bootstrap current is needed as an input in the MHD equilibrium calculation. Thus, an iterating method to calculate an equilibrium with a self-consistent bootstrap current was developed as follows[68, 69]. First, the finite beta equilibrium is

calculated by using the VMEC code with the net toroidal current, $I(s)$, equal to zero. Then using the magnetic fields found by the VMEC code, we calculate the bootstrap current, $I_b(s)$. This current is then input to the VMEC code and a new finite beta equilibrium is calculated. This procedure is iterated until convergence is achieved.

The variation of the bootstrap current depending on the collisionality were studied for the LHD standard configuration[70] with the profiles of the temperature and the density

$$T_e = T_i = T_0(1-s), \quad n_e = n_i = n_0(1-s), \quad (3.50)$$

where subscripts 'e' and 'i' denote the values of electrons and ions, respectively. In the study, two sequences of equilibrium is considered in increasing the beta value for the same pressure profile. One is the temperature sequence where the temperature is increased with the density fixed at $n_0 = 0.2 \times 10^{20}\mathrm{m}^{-3}$. The other one is the density sequence where the density is increased with the temperature fixed at $T_0 = 0.5\mathrm{keV}$. The bootstrap current was evaluated by using eq.(3.35). The magnetic field was assumed to be $B_0 = 1\mathrm{T}$ in both sequences.

Figure 3.4.4 shows the profiles of the geometrical factors normalized by G_b^{tok} in the $1/\nu$ and the plateau regimes. In the vacuum configuration, $G_b^{1/\nu}$ is positive in the whole region, while G_b^{pl} has negative value except the vicinity of the magnetic axis. This property is almost kept at $\beta_0 = 6.4\%$ for both sequences. The total bootstrap currents given by eq.(3.35) in the two sequences are shown in Fig.3.4.5. The positive value in the figure corresponds to the net toroidal current flowing in the direction so as to increase the rotational transform. In the temperature sequence, the positive bootstrap current is enhanced as the beta value grows. On the other hand, in the density sequence, the total bootstrap current is enhanced in the positive direction up to $\beta_0 = 4\%$; however, the absolute value is much less than that in the temperature sequence. The current is reduced beyond $\beta_0 = 4\%$ and becomes negative for $\beta_0 \geq 6\%$. That is, the total bootstrap current reverses the direction. Figure 3.4.6 shows the bootstrap current density at $\beta_0 = 6.4\%$ given by eq.(3.36). The current density in the temperature sequence is always positive, while in the density sequence the bootstrap current density reverses partially in the radial direction.

Figure 3.4.7 shows the normalized collision frequency ν_* defined by eq.(3.48). In the temperature

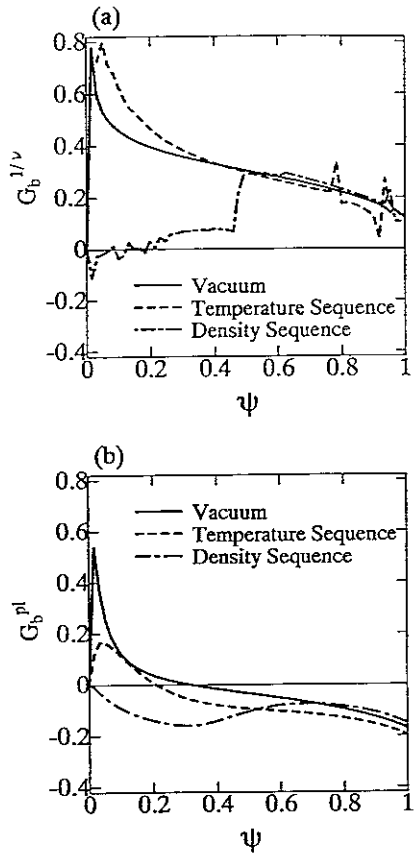

Fig.3.4.4 Profiles of normalized geometrical factors in the limit of (a) $1/\nu$ and (b) plateau regimes in LHD with $B_0 = 1\mathrm{T}$. Solid lines show the values in the vacuum configuration. Dashed and dot-dashed lines show the values at $\beta_0 = 6.4\%$ with $T_0 = 4\mathrm{keV}$, $n_0 = 0.2 \times 10^{20}\mathrm{m}^{-3}$ in the temperature sequence and with $T_0 = 0.5\mathrm{keV}$, $n = 1.6 \times 10^{20}\mathrm{m}^{-3}$ in the density sequence, respectively. ψ denotes the normalized toroidal flux. [70]

sequence the collision frequency becomes small as the beta value increases, and $\nu_* < 10^{-1}$ in the almost all region of the plasma column at $\beta_0 = 6.4\%$ where the temperature is $T_0 = 4.0\mathrm{keV}$. Hence, the collisionality of the plasma is in the $1/\nu$ regime and $G_b^{1/\nu}$ has a dominant effect in the connection formula (3.49) rather than G_b^{pl}. In this sequence, $G_b^{1/\nu}$ is always positive and the profile is insensitive to the beta value as shown in Fig.3.4.4(a). It accounts for the large positive bootstrap current.

On the other hand, the plasma in the density sequence becomes more collisional as beta grows. As shown in Fig.3.4.7, ν_* is larger than unity at $\beta_0 = 6.4\%$ where the density is $n_0 = 1.6 \times 10^{20}\mathrm{m}^{-3}$. There-

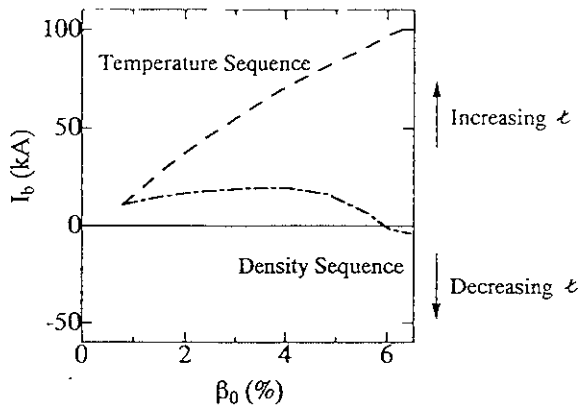

Fig.3.4.5 Total bootstrap currents versus β_0 in the temperature sequence (dashed line) and the density sequence (dot-dashed line). [70]

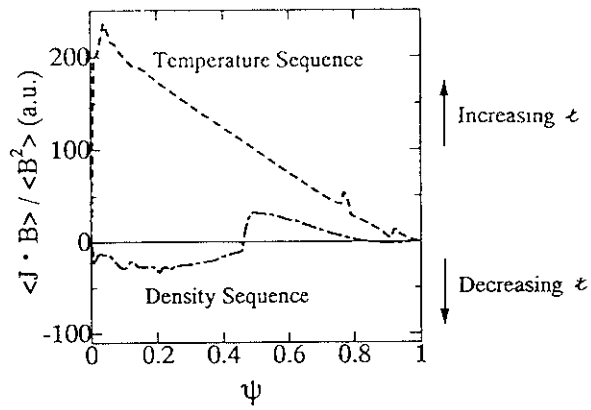

Fig.3.4.6 Profiles of the bootstrap current density. Dashed and dot-dashed lines correspond to the same lines in Fig.3.4.4, respectively. ψ denotes the normalized toroidal flux. [70]

fore, the contribution of G_b^{pl} in the connection formula is larger than that of $G_b^{1/\nu}$. At this beta value, G_b^{pl} is negative in the whole plasma region and has a comparable absolute value with $G_b^{1/\nu}$. Hence, the total bootstrap current reverses the direction due to mainly the negative G_b^{pl} for $\beta_0 \geq 6\%$. However, the effect of the change in the profile of $G_b^{1/\nu}$ cannot be neglected. The reduction of $G_b^{1/\nu}$ in the central region shown in Fig.3.4.4(b) almost coincides with the the negative current density region. Therefore, the reduction of the positive $G_b^{1/\nu}$ in the central region also contributes to the reverse of the direction of the total bootstrap current in the density sequence of the LHD equilibrium.

As is discussed in Sec.3.4.1, the peaked net toroidal current flowing so as to increase the rotational transform is unfavorable with respect to the stability against the interchange mode and vice versa. This tendency is also seen in the case of the bootstrap current. Figure 3.4.8 shows the Mercier unstable regions for the temperature and the density sequences. In the temperature sequence, there exists a large unstable region in the plasma column in Fig.3.4.8(a) and the value of D_I is enhanced as the beta value grows. This is because the magnetic well and the magnetic shear are suppressed due to the small Shafranov shift. An unstable region is also seen in the density sequence in Fig.3.4.8(b), however; the value of D_I is small. Furthermore, the second stability region for the Mercier criterion appears at lower beta value than that in the corresponding currentless equilibrium sequence shown in Fig.3.1.4(a). This is because the local bootstrap current density is already negative in the central region of the plasma even at the beta value where the total bootstrap current is slightly positive as shown in Fig.3.4.6.

The equilibrium with self-consistent bootstrap current is also calculated with the HINT code[71]. In this case,

$$\frac{\partial \boldsymbol{B}}{\partial t} = \nabla \times \left[\boldsymbol{V} \times \boldsymbol{B} - \eta_a \left(\boldsymbol{J} - \frac{\langle \boldsymbol{J}_b \cdot \boldsymbol{B} \rangle}{\langle B^2 \rangle} \boldsymbol{B} \right) \right] \quad (3.51)$$

is used instead of eq.(2.18) to include the effect of the bootstrap current. The procedure for the self-consistent bootstrap current is similar to the case in the VMEC code. The obtained bootstrap current for the LHD plasma shows a good agreement with the VMEC code results.

3.4.4 Internal kink mode in heliotron plasmas

When the net toroidal current flows in the plasma column, it is possible that the current driven mode should be unstable. In the ideal stability analysis, the current driven mode is classified into the internal kink mode and the external kink mode. Both modes are found numerically in the heliotron plasmas.

An internal kink mode can be unstable at $\beta = 0\%$ when there exist two resonant surfaces with the same

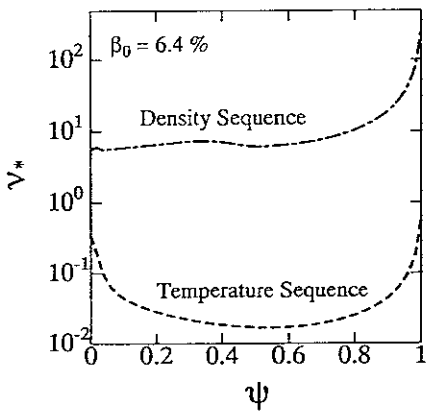

Fig.3.4.7 Profiles of normalized collision frequency. Dashed and dot-dashed lines correspond to the same lines in Fig.3.4.4, respectively. ψ denotes the normalized toroidal flux. [70]

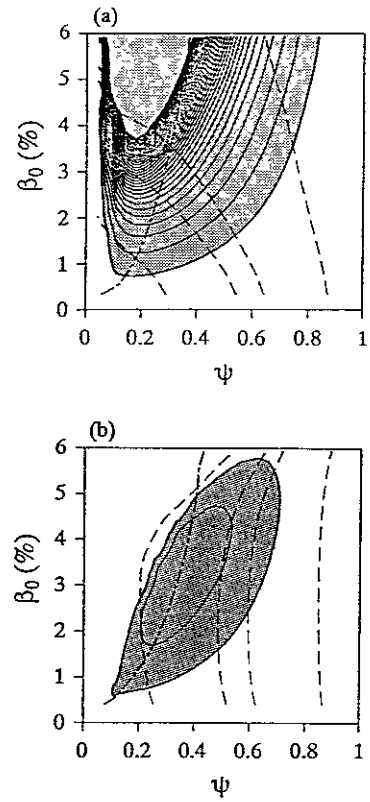

Fig.3.4.8 Mercier unstable regions for (a) temperature sequence and (b) density sequence in the (β_0, ψ) plane. Shaded regions show unstable regions. Solid lines in these regions are the contours of the level surface of D_I which differ by $\Delta D_I = 0.2$. In (a) the contours with $D_I > 8.0$ are not plotted because they are too dense. Dot-dashed line shows the boundary between the magnetic well and hill regions. Dashed lines indicate the positions of the rational surfaces corresponding to $\iota = 1$, 3/4, 2/3 and 1/2 from right to left. ψ denotes the normalized toroidal flux. [70]

rotational transform. As the positive total current I increases, the rotational transform near the magnetic axis increases in the LHD standard configuration, as shown in Fig.3.4.1. There are two surfaces with $\iota = 1$ in the plasma column at $I = 300$kA for $B_0 = 3$T. In this case, an unstable internal kink mode is unstable under the fixed boundary condition. Figure 3.4.9 shows the stream function of the $n = 1$ mode obtained with the RESORM code for $I = 300$kA. The dominant poloidal component is $m = 1$ and the typical structure of the $m = 1$ internal kink mode is seen, which is localized between the magnetic axis and the inner $\iota = 1$ surface.

This property can be understood by evaluating the energy principle in the linear analysis. The potential energy derived from the reduced MHD equations at $\beta = 0$ under the assumption of the straight stellarator configuration is given by

$$\delta W = (2\pi B_0^2/R_0^2) \int [(f\xi')^2 + g\xi^2] dr, \qquad (3.52)$$

$$f = r^3\nu^2, \quad \nu = \iota - n/m, \quad \iota = \iota_h + \iota_J, \qquad (3.53)$$

$$g = r\nu[(m^2-1)\nu - 3r\iota_h' - r^2\iota_h''], \qquad (3.54)$$

where ξ is the radial displacement of plasma which is given by $\xi = (1/r)\partial\Phi/\partial\theta$. Here, ι_h and ι_J denote the rotational transform component generated by the helical coils and the net toroidal current, respectively. The internal kink mode can be unstable when $g < 0$ because δW can be negative. Since both ι_h' and ι_h'' are positive in heliotron configurations, $g < 0$ if $\nu > 0$ for $m = 1$. Thus, the $m = 1/n = 1$ mode can be unstable where $\iota > 1$. There are two regions with $\iota > 1$ in the plasma column in the case where two $\iota = 1$ surfaces exist, that is, the regions between the magnetic axis and the inner $\iota = 1$ surface and the region between the outer $\iota = 1$ surface and the plasma edge. In the former region, the displacement vector which is constant in the radial direction except the region around the inner $\iota = 1$ surface can make the potential energy negative like the internal kink mode in tokamaks[72]. However, the mode localized in the latter region cannot be unstable, because the gradient of ξ is necessary near the edge to satisfy

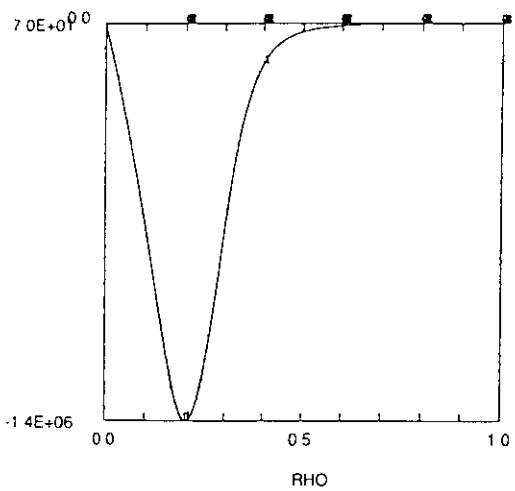

Fig.3.4.9 Fourier components of the $n = 1$ stream function in the LHD configuration with $I = 300$kA. Dominant component is $m = 1/n = 1$ mode.

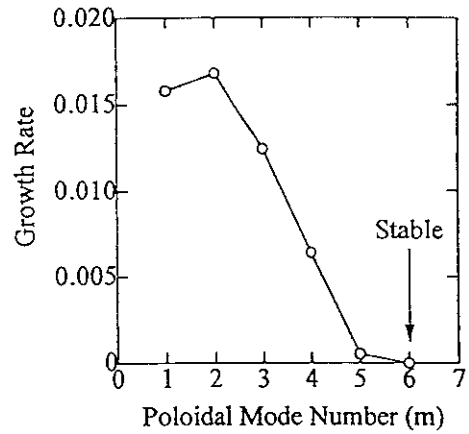

Fig.3.4.10 Dependence of the growth rate of the internal kink mode on the poloidal mode number m in the LHD configuration with $I = 300$kA.

the fixed boundary condition which has a stabilizing contribution. Thus, the structure of the internal kink mode in the heliotron plasma is localized in the inside of the inner $\iota = 1$ surface, as shown in Fig.3.4.9.

Besides, eq.(3.54) suggests that the modes with $m \geq 2$ can be unstable if $0 < \nu < (3r\iota_h' + r^2\iota_h'')/(m^2 - 1)$, which cannot be unstable in the straight tokamaks. Actually, the modes with $m \geq 2$ are obtained numerically in the $I = 300$kA case. The $m = n$ component is dominant for the each mode and the mode structure is localized in the inside of the inner $\iota = 1$ surface, as is in the $m = 1$ mode. As shown in Fig.3.4.10, the growth rate decreases as m increases, and the modes with $m \geq 6$ are stable in this case. This tendency is consistent with eq.(3.54).

In the finite beta current carrying plasma of Heliotron E, a hybrid mode of the internal kink mode and the interchange mode are destabilized[73]. When the current profile is chosen to be highly peaked such as $J = J_0(1 - s)^{10}$, the zero beta equilibrium of the Heliotron E also has two $\iota = 1$ surfaces in the plasma column with a small total current. In this case, the $m = 1/n = 1$ internal kink mode is destabilized in the inside of the inner $\iota = 1$ resonant surface at $\beta_0 = 0\%$ as shown in Fig.3.4.11(a), where the radial component of the displacement vector calculated with the KSTEP code is shown. As β is increased with the pressure profile of $P = P_0(1 - s)^2$, the $m = 1/n = 1$ interchange mode becomes unstable as well as the internal kink mode, which is resonant at the outer $\iota = 1$ surface. At $\beta_0 = 6\%$, as shown in Fig.3.4.11(b), the contribution of the interchange mode to the total potential energy becomes comparable with that of the internal kink mode, and beyond the beta value, the interchange mode becomes dominant.

3.4.5 External kink mode in heliotron plasmas

In Sec.3.4.3, the effects of the bootstrap current on the interchange mode was discussed. It was also studied how the bootstrap current drives the external kink mode by means of the free-boundary version of the KSTEP code in the LHD standard configuration[74].

The external kink mode is found in the temperature sequence in Sec.3.4.3, where the self-consistent bootstrap current flows so as to increase the rotational transform as the beta value increases. Figure 3.4.12 shows the growth rates for the fastest growing free-boundary modes of $n = 1$, 2 and 3 with the conducting wall at infinity. In the region of $\langle\beta\rangle < 2\%$ where the equilibrium is Mercier unstable as shown in Fig.3.4.8(a), the unstable modes shows the interchange type, i.e., they are localized around the resonant surfaces inside the plasma column and the influence of the free boundary is weak. As the beta value increases beyond 2%, the mode becomes much more global and loses its resonance character. Figure 3.4.13 shows the Fourier component of the $n = 1$ mode at

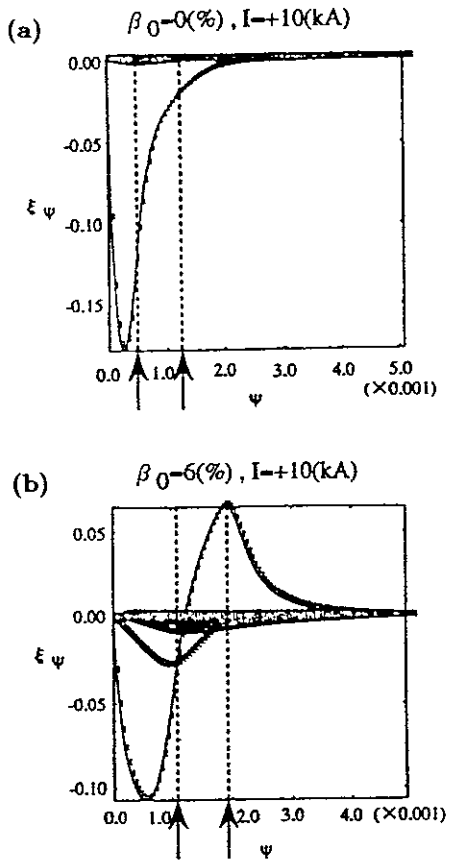

Fig.3.4.11 Displacement vector of the $n = 1$ mode for the current carrying Heliotron E equilibria at $\beta_0 = 0\%$ (top) and 6% (bottom). Here, ψ means the poloidal magnetic flux. The arrows denote the position of the $\iota = 1$ surface. [73]

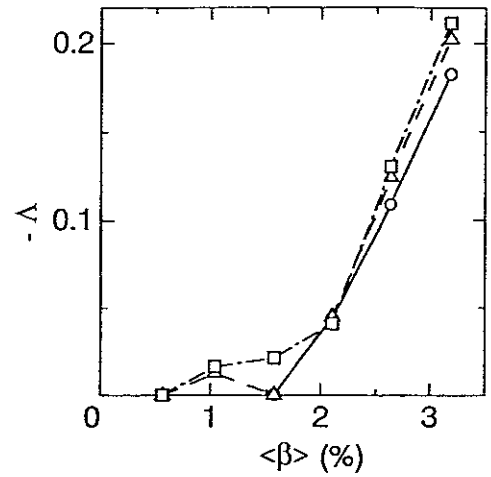

Fig.3.4.12 Unstable eigenvalues, $-\Lambda$ for the fastest growing free-boundary low-n modes for the standard LHD configuration with a self-consistent bootstrap current with the conducting surface at $b = \infty$ as functions of the average β. The circles denote growth rates for the $n = 1$ mode, the triangles for the $n = 2$ mode, and the squares for the $n = 3$ mode. [74]

$\langle\beta\rangle = 3.18\%$, which shows a structure of the external kink mode. The $n = 2$ and $n = 3$ modes have the similar structure. The dominant component is the mode with the poloidal mode number such that $m = n$ for each n, because the rotational transform at $\langle\beta\rangle = 3.18\%$ is just above unity almost whole region of the plasma column as shown in Fig.3.4.14.

In order to know which is the dominant driving term in the potential energy, the current-driven term or the pressure-driven term, a calculation with the pressure driven contribution to the potential energy ignored in eq.(2.26) and a calculation with the correct pressure distribution with $J_\zeta = 0$ were carried out. Either calculation shows that an instability exists with a smaller growth rate than that for the full potential energy, and the growth rates of the two cases are comparable. This demonstrates that both kink and interchange driven terms are important in eq.(2.26), because the equilibrium not only carries a large net toroidal current but also is strongly Mercier unstable.

In the no net current case, another type of the free boundary mode can be unstable in the LHD standard configuration[74]. The $n = 1$ and $n = 2$ modes are destabilized with the conducting wall at infinity for $\langle\beta\rangle \simeq 3\%$. The growth rate is considerably smaller than in the bootstrap current case, but it is still large. This mode has following properties. The mode structure, shown in Fig.3.4.15, is global and many sidebands have comparable amplitude. As is expected from the Mercier stability diagram of Fig.3.1.4(a), the mode is stabilized when the conducting wall is set at the plasma surface. The growth rate of the $n = 1$ case is reduced considerably if the current driven term in δW is ignored, but it is almost unchanged if the pressure driven term is eliminated. Thus, the Pfirsch-Schlüter current is responsible for the instability. Similar instability is obtained in the ATF configuration as well[75].

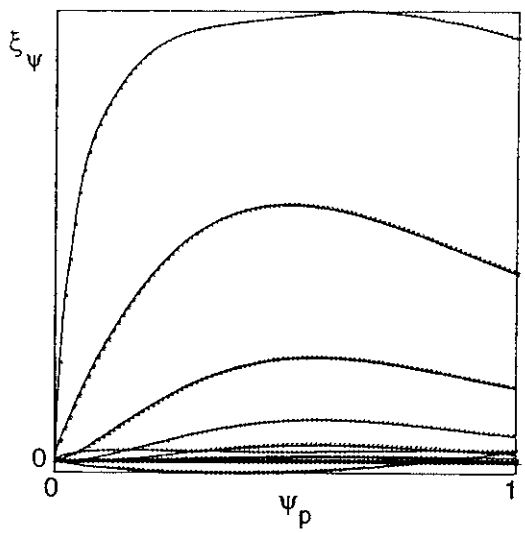

Fig.3.4.13 Fourier components of the displacement vector perpendicular to the magnetic surfaces, ξ_ψ, for the fastest growing free-boundary mode with a toroidal mode number $n = 1$ for a configuration with a self-consistent bootstrap current with $\langle\beta\rangle = 3.18\%$; $\Lambda = -0.182$. Here, ψ_p means the normalized poloidal magnetic flux. The dominant poloidal mode number is $m = 1$, but other contributions are equally important. As $\langle\beta\rangle$ has been increased the mode has become much more global in nature, being driven by both kink and interchange effects. [74]

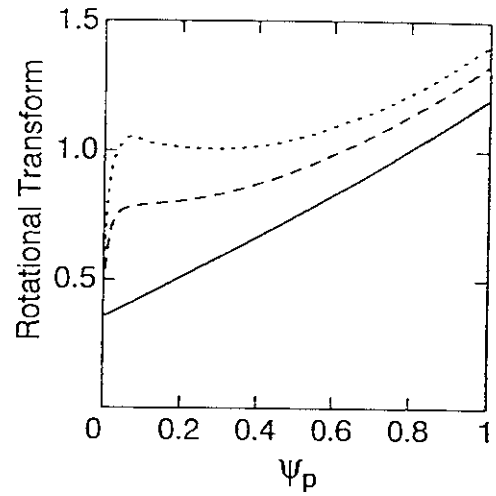

Fig.3.4.14 The rotational transform as a function of the poloidal flux for the standard LHD configuration if a self-consistent bootstrap current is introduced as β is increased. The current, calculated for a low-density sequence, adds to the transform provided by the helical structure. The solid curve is for $\langle\beta\rangle = 0$, the dashed curve is for $\langle\beta\rangle = 1.57\%$, and the dotted curve is for $\langle\beta\rangle = 3.18\%$. Here, ψ_p means the normalized poloidal magnetic flux. [74]

3.5 Ballooning modes

3.5.1 Local mode analysis

The ballooning mode is a crucial instability in high beta tokamak plasmas, and therefore, the analysis in the axisymmetric configuration has been extensively progressed. As is in the tokamak case[76], the ordinary differential equation along the field line which is called a high-n ballooning equation can be derived for the ballooning mode in the three-dimensional configuration. The high-n ballooning equation is derived for the mode with $k_\perp/k_\parallel << 1$ in the covering space (ψ, η, α)[77]. Here ψ denotes the label of the magnetic flux, η is the coordinate along the field line and α is the label of the field line on a flux surface. When flux coordinates (ψ, θ, ζ) are employed, where θ and ζ are the poloidal and the toroidal angles, respectively, the η and α are defined as

$$\eta = \theta, \quad \alpha = \zeta - \theta/\epsilon. \tag{3.55}$$

It is noted that η is defined on the infinite domain, i.e., $-\infty < \eta < \infty$ in the ballooning space, while $0 \leq \theta \leq 2\pi$. Here we employ the Boozer coordinates[54] as the flux coordinates. Then, the magnetic field is expressed as

$$\boldsymbol{B} = \nabla\alpha \times \nabla\psi. \tag{3.56}$$

For the mode with $k_\perp/k_\parallel << 1$, we can introduce an eikonal expression for the displacement vector given by

$$\boldsymbol{\xi} = \hat{\boldsymbol{\xi}} \exp\left[i\frac{S(\psi,\alpha)}{\epsilon} - i\omega t\right], \tag{3.57}$$

where S is an eikonal which is related to the perpendicular wave vector as $\boldsymbol{k}_\perp = \nabla S$. An ordering parameter ϵ is introduced to indicate a large $k_\perp$. The lowest order of the linearized MHD equations in ϵ gives the high-n ballooning equation for $\xi \equiv \hat{\boldsymbol{\xi}} \cdot \nabla\psi$ for given ψ and α, which is written as

$$\begin{aligned} &\boldsymbol{B}\cdot\nabla\left[\frac{|\boldsymbol{k}_\perp|^2}{B^2}\boldsymbol{B}\cdot\nabla\xi\right] \\ &+\frac{2}{B^4}\boldsymbol{B}\times\boldsymbol{k}_\perp\cdot\boldsymbol{\kappa}\boldsymbol{B}\times\boldsymbol{k}_\perp\cdot\nabla P\xi \\ &+\rho_m\omega^2\frac{|\boldsymbol{k}_\perp|^2}{B^2}\xi = 0, \end{aligned} \tag{3.58}$$

where the incompressibility is assumed. Here the first term is the field line bending term which has a sta-

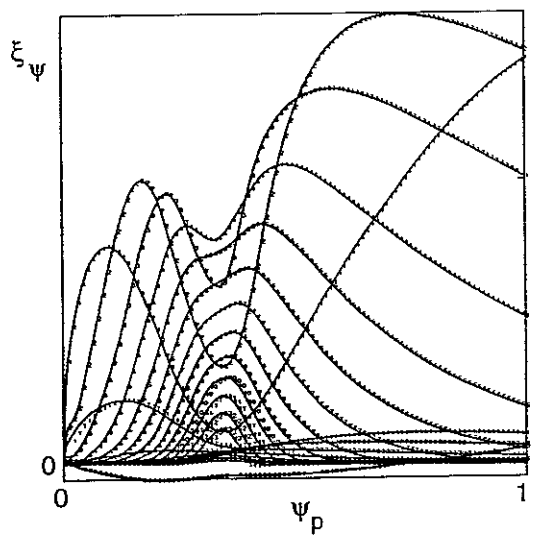

Fig.3.4.15 Fourier components of the displacement vector perpendicular to the magnetic surfaces, ξ_ψ, for the fastest growing free-boundary mode with a toroidal mode number $n = 1$ for a configuration with no toroidal current with $\langle\beta\rangle = 3.18\%$; $\Lambda = -5.21 \times 10^{-2}$. Here, ψ_p means the normalized poloidal magnetic flux. The dominant poloidal mode number is $m = 1$. This mode would almost be stable if the vacuum vessel were treated as being perfectly conducting. [74]

bilizing contribution, while the second term is the driving term of the instability.

The model of interest is a low-beta tokamak equilibrium with the pressure which has a steep gradient only in the vicinity of a magnetic surface. If a large aspect ratio and a circular cross section are assumed, the ballooning equation eq.(3.58) is reduced to[78]

$$\frac{\partial}{\partial\theta}\left[(1+\Lambda^2)\frac{\partial\xi}{\partial\theta}\right] + \alpha(\Lambda\sin\theta + \cos\theta)\xi = 0, \quad (3.59)$$

in the cylindrical coordinates (r, θ, ϕ). Here Λ is defined as

$$\Lambda(\theta) = \int_0^\theta \hat{s}\, d\theta \quad (3.60)$$

with the local magnetic shear, $\hat{s}$, given by

$$\hat{s} = \bar{s}_T - \alpha_\beta \cos\theta, \quad (3.61)$$

where $\bar{s}_T$ and α_β represent a global shear in tokamaks and a measure of the pressure gradient which are defined with the safety factor $q = 1/\iota$ as,

$$\bar{s}_T = \frac{r}{q}\frac{dq}{dr}, \quad \alpha_\beta = -q^2 R_0 \frac{d\beta}{dr}, \quad (3.62)$$

respectively. Substituting eq.(3.61) into eq.(3.60), Λ is expressed as

$$\Lambda(\theta) = \bar{s}_T\theta - \alpha_\beta \sin\theta. \quad (3.63)$$

It is noted that $\bar{s}_T$ is positive in the standard tokamaks and α_β is also positive in the usual pressure profile. Hence, Λ becomes small in the vicinity of $\theta \simeq 0$ if $\alpha_\beta \sim \bar{s}_T$. In this case, the line bending stabilizing term in eq.(3.59) is reduced, and therefore, the ballooning mode can be destabilized.

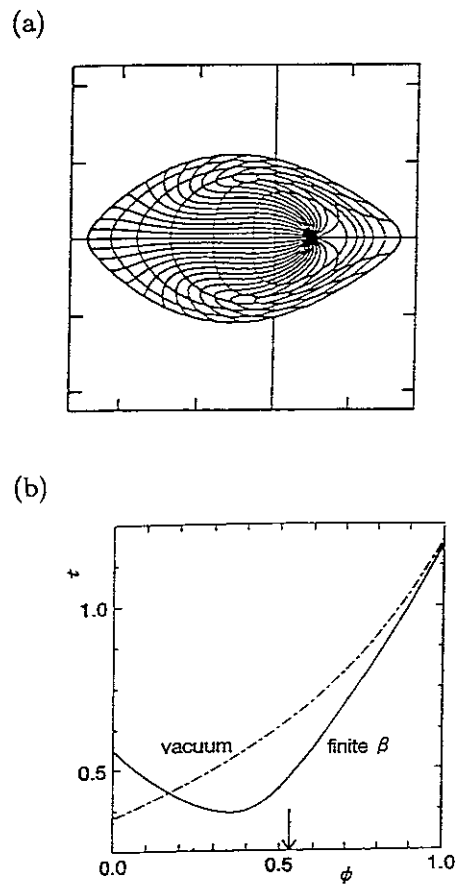

Fig.3.5.1 (a) Equally spaced (ψ, θ) mesh of the Boozer coordinates of a horizontally-elongated cross section and (b) the profiles of the rotational transform of the currentless LHD equilibrium under the fixed boundary with $P = P_0(1-\psi)^2$ at $\beta_0 = 8\%$ in the standard configuration. Here, ψ means the normalized toroidal magnetic flux. [81]

On the contrary, in heliotron configurations, $\bar{s}_T$ is usually negative and Λ cannot be reduced in eq.(3.63) because $dq/dr < 0$ in the vacuum configuration. Hence, it was speculated that the heliotron plasma

would be stable against the ballooning mode[79]. However, it was shown that eq.(3.58) can have unstable eigenmodes in the ATF[80] and the LHD[81] three-dimensional equilibria. Figure 3.5.1(a) shows a poloidal cross section with (ψ, θ) grids in the Boozer coordinates of a currentless LHD equilibrium at $\beta_0 = 8\%$[81], which is calculated with the VMEC code with the pressure profile of $P = P_0(1-s)^2$. The rotational transform in this equilibrium is shown in Fig.3.5.1(b). At the surface pointed by the arrow in the figure, an unstable high-n ballooning mode is obtained which has a structure shown in Fig.3.5.2.

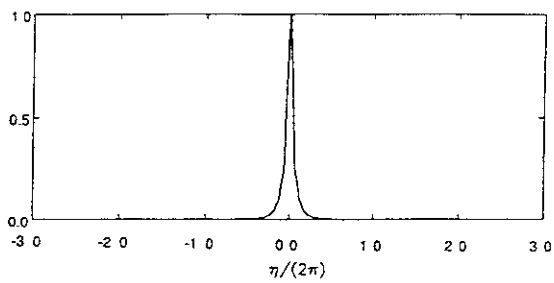

Fig.3.5.2 Eigenfunction of the high-n ballooning mode along the field line with $(\theta_k = 0, \alpha = 0)$ at the surface indicated by the arrow in Fig.3.5.1(b). [84]

The mechanism of the destabilization of the ballooning mode in the region with positive $\epsilon'(\psi)$ can be understood by the consideration about the local magnetic shear[81, 82, 83]. In the line bending term of eq.(3.58), the square of the perpendicular wave vector under the currentless condition in the Boozer coordinates is given by

$$|\boldsymbol{k}_\perp|^2 = \frac{2\psi}{B_0 g_{\theta\theta}} \left\{ 1 + g_{\theta\theta} \left(\frac{|\nabla\psi|^2}{\psi} \right)^2 \Lambda \right\}, \qquad (3.64)$$

where g_{ij} is a covariant metric in the Boozer coordinates. The local magnetic shear $\hat{s}$ in the three-dimensional configurations is given by

$$\hat{s} = \bar{s} + \tilde{s}, \qquad (3.65)$$

where the global magnetic shear $\bar{s}$ and the oscillatory part of the local shear $\tilde{s}$ are defined by

$$\bar{s} = \frac{\psi}{\epsilon} \frac{d\epsilon}{d\psi}, \quad \tilde{s} = \frac{\partial}{\partial\eta} \left(\psi \frac{g_{\psi\theta}}{g_{\theta\theta}} \right), \qquad (3.66)$$

respectively. In this case, Λ has the form of

$$\Lambda = \int_{\theta_k}^{\eta} \hat{s} d\eta \qquad (3.67)$$

$$= \bar{s}(\eta - \theta_k) + \psi \frac{g_{\psi\theta}}{g_{\theta\theta}}, \qquad (3.68)$$

with $\theta_k \equiv k_\psi / k_\alpha$ where $k_\psi = \partial S/\partial\psi$ and $k_\alpha = \partial S/\partial\alpha$.

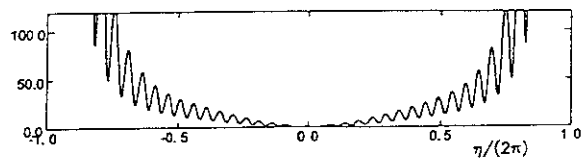

Fig.3.5.3 Profile of $|\boldsymbol{k}_\perp|^2$ along the field line with $(\theta_k = 0, \alpha = 0)$ at the surface indicated by the arrow in Fig.3.5.1(b). [81]

The sign of the metric $g_{\psi\theta}$ is related to the angle between the ψ-constant and θ-constant lines in the poloidal cross section. In the equilibrium with large Shafranov shift as shown in Fig.3.5.1(a), sharp bends of the θ-constant lines in the Boozer coordinates can be seen at a flux surface in the outward region of the torus. We call the surface turning surface, where $g_{\psi\theta} = 0$. The turning surface roughly corresponds to the minimum point of the rotational transform in Fig.3.5.1(b). Outside the turning surface, $g_{\psi\theta}$ in $\bar{s}$ can be approximated as $c \sin\theta$ with negative c. In this region, the global magnetic shear $\bar{s}$ is positive. Therefore, the local magnetic shear can be reduced even in the region with positive $\epsilon'(\psi)$. The reduction of the local magnetic shear leads to the substantial degradation of $|\boldsymbol{k}_\perp|^2$ around $\eta = \theta_k$ as shown in Fig.3.5.3. Then, the stabilizing effects in the line bending term is reduced and the high-n ballooning mode is destabilized of which mode structure is shown in Fig.3.5.2.

In order to investigate the property of the high-n ballooning modes in heliotron configurations, we consider the local curvature of the field line in the second term of eq.(3.58) as well as the local shear. In tokamaks, the curvature is attributed to only the toroidicity, and the field line has no α-dependence. On the other hand, the local magnetic curvature in the heliotron equilibria consists of both the toroidal curvature and the helical curvature. This results in the fact that the local curvature is the most unfavorable at the outside region of the torus in the horizontally

elongated cross section, while the curvature is locally favorable even at the outside region in the vertically elongated cross section. Thus, the local magnetic curvature outside of the torus strongly depends on the label of the field line, α.

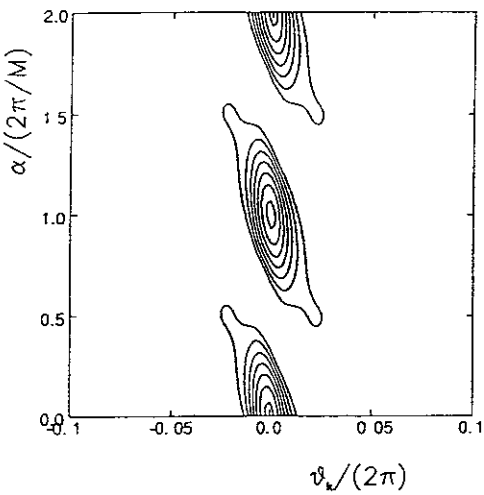

Fig.3.5.4 Contour of the eigenvalue ω^2 in (θ_k, α) plane at the surface indicated by the arrow in Fig.3.5.1(b). [84]

The ballooning mode can be unstable even in the Mercier stable region because it can be localized only in the region with the unfavorable curvature[84]. In this case, the high-n ballooning modes become unstable only in the high beta equilibrium which has a large Shafranov shift and the turning surface in the plasma column so as to reduce the local magnetic shear sufficiently. The mode structure is strongly localized around $\eta = \theta_k$ because the secular term in $|\boldsymbol{k}_\perp|^2$ is amplified by the large Shafranov shift through the factor of $|\nabla\psi|$ beyond $\eta = 2\pi$ as shown in Fig.3.5.2. As the local magnetic curvature has a strong dependence on α, the eigenvalue also strongly depends on α, i.e., $\omega^2 = \omega^2(\psi, \alpha, \theta_k)$. As shown in Fig.3.5.4, the topology of the level surfaces of unstable ω^2 is spheroid in the space of (ψ, α, θ_k). On the contrary, since the eigenvalue does not depend on α in tokamaks, i.e., $\omega^2 = \omega^2(\psi, \theta_k)$, the level surfaces should be cylindrical and the method of quantum condition can be used to compose a global mode structure[76].

In the Mercier unstable region. there always exists the unstable high-n ballooning mode. This type of the ballooning mode is obtained in the currentless LHD equilibrium with a broad pressure profile of

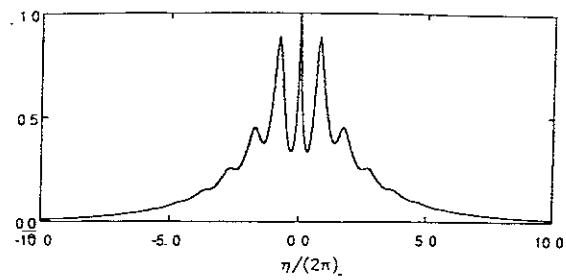

Fig.3.5.5 Eigenfunction of the high-n ballooning mode along the field line with $(\theta_k = 0, \alpha = 0)$ in the strongly Mercier unstable region of the LHD equilibrium with $P = P_0(1-\psi^2)^2$. [84]

$P = P_0(1-s^2)^2$[84]. In this region, $|\boldsymbol{k}_\perp|^2$ need not be so much modified for the destabilization of the high-n ballooning mode as that in the Mercier stable equilibria, because the average magnetic curvature is already unfavorable along the field line. Therefore, there can exist not only the mode strongly localized in the region with the unfavorable local curvature as is in the Mercier stable region, but also the mode with extended structure along the field line which is destabilized by the unfavorable averaged curvature in the region as shown in Fig.3.5.5. The eigenvalue of the latter mode is smaller than that of the former modes, because the eigenfunction passes both the unfavorable and the favorable local curvature regions. Thus, the dependence of the eigenvalues of the latter modes on α is weak, while the eigenvalues in the former modes strongly depend on α. Hence, the level surfaces of the eigenvalue of the mode in the Mericier unstable region present the two types of topological structure in the (ψ, α, θ_k) space. That is, there exist the level surfaces of small ω^2 corresponding to the mode with the extended structure along the field line which would be continuous in α direction, or nearly cylindrical, and the spheroidal structures with large ω^2 corresponding to the strongly localized mode structure exist inside the continuous surface.

3.5.2 Global mode analysis

The eigenmode of eq.(3.58) is a quasimode not a normal mode. A technique based on a quantum condition which gives a relation between the quasimode and the normal mode is established in the tokamak configuration[76], where the eigenvalue is indepen-

dent of α. In the heliotron configurations, however, the unstable mode as a solution of eq.(3.58) is not directly related to the global normal mode. Therefore, it has been extensively studied by means of the three-dimensional numerical codes how the unstable mode obtained by the local mode analysis is related to the global normal mode. Particularly, the analysis for the modes in the Mercier unstable region is progressed.

As is seen in the previous section, the eigenvalue ω^2 of the local ballooning mode is a function of q, α and θ_k, i.e., $\omega^2 = \lambda(q, \alpha, \theta_k)$. Here, q is used for the label of the magnetic surface instead of ψ. In the (q, α, θ_k) space, the ray corresponding to $S = const.$ on the level surface of ω^2 gives information about the eigenvalue of the corresponding normal mode[77, 85]. Employing the method of the characteristics, the ray equations are given by

$$\dot{\alpha} = -\theta_k \frac{\partial \lambda}{\partial \theta_k} \tag{3.69}$$

$$\dot{q} = \frac{\partial \lambda}{\partial \theta_k} \tag{3.70}$$

$$\dot{\theta}_k = \theta_k \frac{\partial \lambda}{\partial \alpha} - \frac{\partial \lambda}{\partial q}, \tag{3.71}$$

where the dot denotes the derivative with respect to dummy time variable parameterizing the characteristics.

The ray was traced in the LHD currentless equilibrium with $P = P_0(1-s^2)^2$ at $\beta_0 = 4\%$[85]. This equilibrium has an Mercier unstable region in the plasma column. Therefore, the level surface of ω^2 has an almost cylindrical structure in this region. Thus, the ray trajectory seems to be wound around the cylinder as shown in Fig.3.5.6. This structure is similar to the one in the axisymmetric plasma, and therefore, the quantum method in the tokamak ballooning mode can be applicable. As the trajectory of the ray is a periodic helical winding in the α axis, the projection of the trajectory on the q-θ_k plane corresponds to a rotation along a closed line. Here we define $\Pi = \Pi(\omega^2)$ as the average increase of α along the ray for one rotation of the projected trajectory. Noting that the toroidal periodicity has to be satisfied in the normal mode and that the eikonal S jumps by $\pi/2$ according to the WKB method when the ray passes each turning point, the relation

$$\Pi(\omega^2) = \frac{2N+1}{2n} \tag{3.72}$$

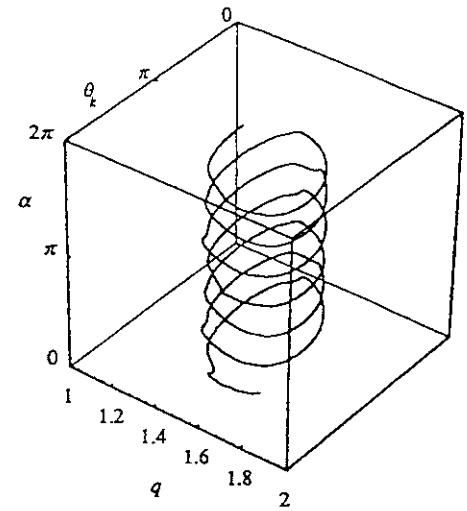

Fig.3.5.6 The ray trajectory in (q, α, θ_k) space in the Mercier-unstable LHD equilibrium. [85]

is derived, where N and n are the radial and the toroidal mode numbers, respectively. This relation indicates that the eigenvalue of the normal mode corresponding to the unstable local ballooning modes of which the level surface of ω^2 has a cylindrical structure shows a discrete spectrum. In the case of the spheroidal structure in the level surface, a continuum band of the eigenvalue is obtained at the center of the spheroid, which corresponds to the limit of $n = \infty$. Figure 3.5.7 shows the solution of eq.(3.72) for $N = 0$, 1 and 2.

In order to examine the validity of this method the global modes were calculated with the TERPSICHORE code in this three-dimensional equilibrium. The eigenvalues are also shown in Fig.3.5.7 for the comparison. In this figure, the three most unstable eigenvalues are plotted for each n. In this calculation, the unstable modes were searched in the range of $2 \simeq n \simeq 14$, and 94 Fourier modes were provided for the perturbation in the space of the poloidal and the toroidal angles. It is easily seen that these three most unstable modes correspond to the modes with $N = 0$, 1 and 2 obtained in the local analysis. The agreement of the eigenvalues between the two methods becomes excellent for large n and N.

The effort to obtain the global mode corresponding to the eigenvalue of which the level surface has the

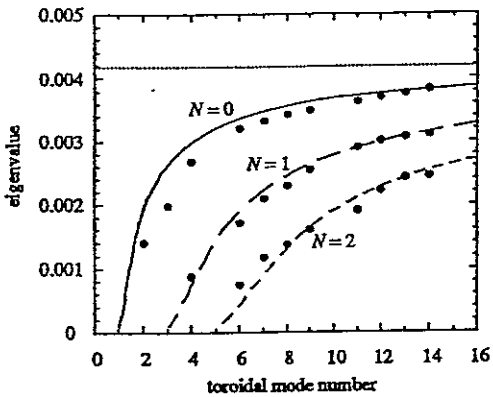

Fig.3.5.7 Comparison of WKB-ballooning growth rate eigenvalue, $-\omega^2$, (curves) with the TERPSICHORE results (dots) plotted versus dominant toroidal mode number n for the first three radial mode numbers, $N = 0, 1, 2$. The dotted horizontal line represents the $n = \infty$ continuum band defined by fixed points of the ray equations. [85]

spheroidal structure in (ψ, α, θ_k) space in the local mode analysis were made with the CAS3D code in the Mercier unstable region of the LHD configuration[86]. The unstable local mode with the spheroidal level surface of the eigenvalue strongly depends on α because it is mainly driven by the localized magnetic curvature in the helical ripples, and therefore, the coupling between the Fourier components in the corresponding global mode with different toroidal mode number should be quite strong. In the LHD configuration, since the rotational transform is almost less than unity, many Fourier components with large n are necessary in the calculation for the sufficient overlap of the components with different n. That is, it is essential to change the Fourier space of the perturbation in the toroidal direction as well as in the poloidal direction in order to examine the dependence of the mode structure on α. In the CAS3D code, the perturbation Fourier modes in the poloidal and the toroidal directions are chosen so as to be distributed around a given dominant mode with $m = M_p/n = N_p$.

The LHD equilibrium with $P = P_0(1-s)^2$ at $\beta_0 = 5.9\%$ under the flux conserving constraint has an Mercier unstable region around the $\iota = 3/5$ surface with the positive global shear $d\iota/ds > 0$. Three cases of the global mode in the equilibrium show quite different properties attributed to the toroidal mode coupling. The first case is for the small toroidal

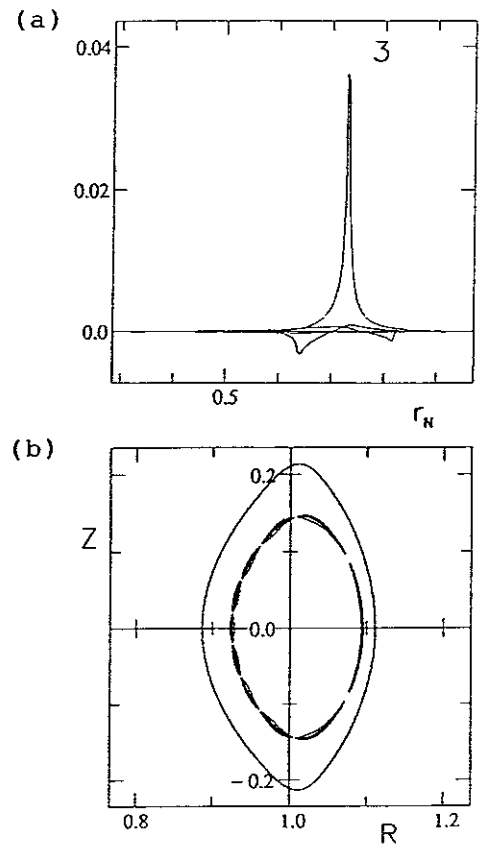

Fig.3.5.8 (a) Profile of the Fourier components of the normal displacement vector $\xi \cdot \nabla\psi$ with the dominant toroidal mode number and (b) the corresponding contours of the perturbed pressure $\tilde{P} = -\nabla P \cdot \xi$ on the vertically elongated poloidal cross section in the calculation with $(M_p, N_p) = (5, 3)$ and $M_{pt} = 151$. Here r_N denotes the average minor radius. [86]

mode numbers, $n < M$, where the number of toroidal field period M is 10 in the LHD. Here $M_p = 5$ and $N_p = 3$ are chosen and 151 Fourier modes(M_{pt}) are distributed around the dominant mode for the perturbation. Figure 3.5.8 shows the Fourier components of the radial displacement, $\xi \cdot \nabla s$, and the level surfaces of the perturbed pressure, $\tilde{P} = -\xi \cdot \nabla P$, of the most unstable eigenmode. The dominant component of the displacement is localized around the resonant surface, and the mode coupling is quite weak in both the poloidal and the toroidal direction. The contour of the perturbed pressure spreads widely in the poloidal direction. These properties of the mode structure indicates that the mode is typical interchange mode

driven by the average component of the magnetic curvature. In this case, the normalized eigenvalue of the global mode is $\omega^2 = -4.99 \times 10^{-5}$.

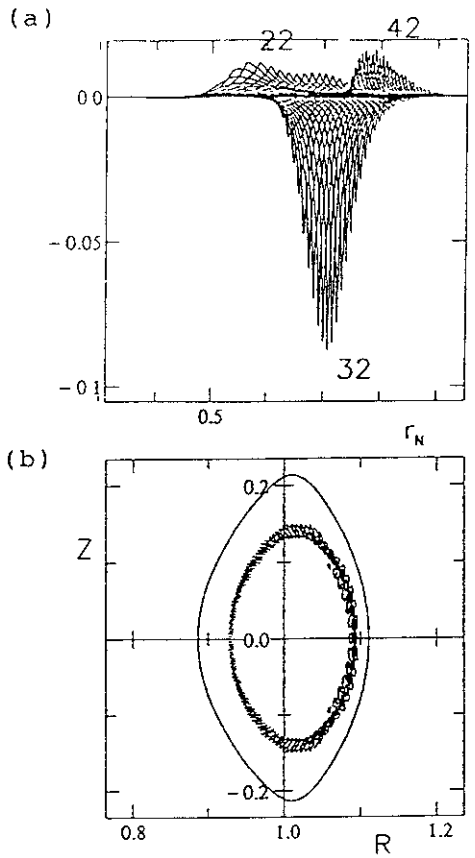

Fig.3.5.9 The same quantities as in Fig.3.5.8 with $(M_p, N_p) = (38, 22)$ and $M_{pt} = 371$. [86]

The second case is for the moderate toroidal mode numbers, $n \sim M$. Here $M_p = 38$ and $N_p = 22$ are chosen and 371 Fourier modes are distributed around the dominant mode for the perturbation. The mode structure is like a tokamak-like ballooning mode as shown in Fig.3.5.9. The radial displacement is composed of three groups of the Fourier modes with different toroidal mode numbers, $n = 22$, $n = 32$ and $n = 42$. The structure results from the weak toroidal mode coupling in the three-dimensional equilibrium. Each group consists of many Fourier modes with different poloidal mode numbers corresponding to the strong poloidal mode coupling. Hence, the perturbed pressure is poloidally localized in the outer region of the torus. It is noted that the dominant group of the Fourier components with $n = 32$ is still localized in the Mercier unstable region. In this case, the normalized eigenvalue of the global mode is $\omega^2 = -1.89 \times 10^{-3}$.

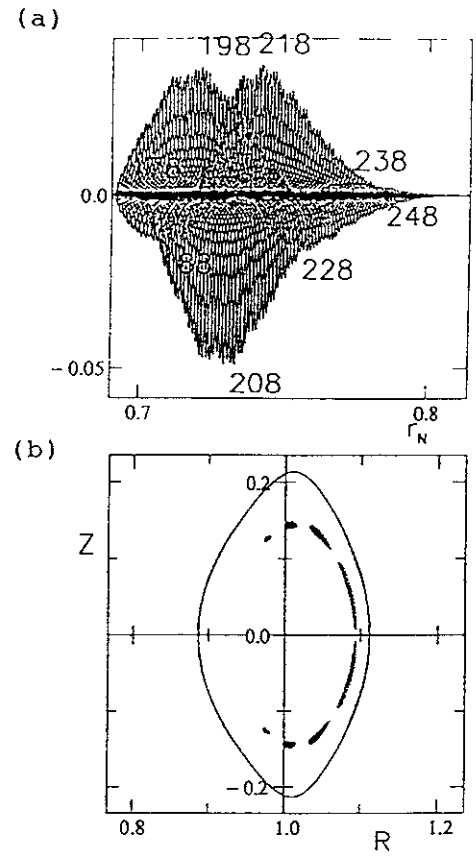

Fig.3.5.10 The same quantities as in Fig.3.5.8 with $(M_p, N_p) = (342, 198)$ and $M_{pt} = 397$. [86]

The last case is for the large toroidal mode numbers, $n >> M$. Here $M_p = 342$ and $N_p = 198$ are chosen and 793 Fourier modes are distributed around the dominant mode for the perturbation. As shown in Fig.3.5.10, the radial displacement has a strong coupling of both the poloidal and the toroidal modes. It is composed of eight groups of the Fourier modes with different toroidal mode numbers. Each group consists of many Fourier modes with different poloidal mode numbers corresponding to the strong poloidal mode coupling as in the second case, however, couples each other strongly. In this structure, the perturbed pres-

sure is localized not only in the outside of torus but also in the top and the bottom region in the vertically elongated cross section where the magnetic curvature is locally unfavorable due to the three-dimensional structure of the equilibrium. Therefore, the mode is a ballooning mode peculiar to the three-dimensional configuration. In this case, the normalized eigenvalue of the global mode is $\omega^2 = -6.32 \times 10^{-3}$.

In the points of the toroidal mode coupling and the property of the localization of the mode structure, the former two cases correspond to the cylindrical structure in the level surface of the eigenvalue in the local mode analysis and the last case to the spheroidal structure. The tendency of the eigenvalue in the global modes also agrees with the results in the local mode analysis because the cylindrical level surfaces is located outside the spherical surfaces, which spreads to the marginal stable region.

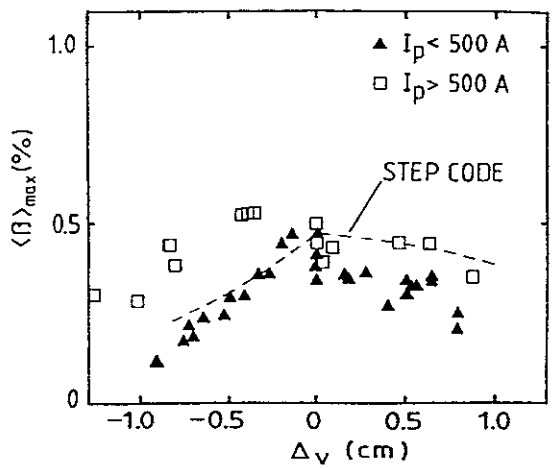

Fig.4.1.1 Experimentally obtained maximum $\langle\beta\rangle$ values (closed triangles) restricted by pressure driven MHD instabilities in currentless Heliotron DR plasmas versus the magnetic axis shift. The critical $\langle\beta\rangle$ values calculated with the KSTEP code are shown as dashed lines. The open squares are the maximum $\langle\beta\rangle$ values obtained in stabilized discharges by applying a small toroidal plasma current. [87]

4 Comparison between Numerical and Experimental Results

In order to know the validity of the theory and the numerical simulation, the comparison of the results with the experimental data is inevitable. Several comparison shows that MHD theoretical analyses explain the experimental results well.

In the Heliotron DR plasma, good agreement in the critical beta value were shown between the experiments and the numerical calculations[87]. In the vicinity of the maximum beta value, the fluctuation of the soft-X ray signal grew in the plasma with small toroidal current. This indicates that the critical beta value was limited by the pressure driven instability. Figure 4.1.1 shows the maximum beta value observed in the experiments and the beta limit by the interchange mode given by the numerical calculation with the KSTEP code as the function of the vacuum axis position Δ_v. In the calculation, the currentless equilibrium with the pressure profile of $P = P_0(1 - \Psi_{eq})^2$ is assumed where Ψ_{eq} denotes the normalized equilibrium poloidal flux. The beta limit given by the numerical calculation agrees well with the experimental data for the whole range of Δ_v. When the net toroidal current was induced in the plasma column by means of the Ohmic coil, the stability was improved as shown in Fig.4.1.1. The stabilizing mechanism can be explained with the theoretical results of Sec.3.4.1. Even in the improved equilibrium with respect to the ideal interchange mode, magnetic fluctuations with high frequency were still observed[88]. They can be attributed to the resistive interchange mode, because the resistive mode can be destabilized in the region where the ideal mode is stable as discussed in Sec.3.3.1. The degradation tendency of the critical beta value due to the interchange modes was also observed in the Heliotron E plasma when the plasma was shifted inward[7].

In the ATF experiments, the dependence of the magnetic fluctuation amplitude on the beta value for the various operation conditions is summarized in Ref.[89]. In this case, the amplitude increases as the beta value is increased up to $\langle\beta\rangle \sim 0.3\%$, however, the amplitude decreases beyond the beta value. It means that there exists the feature of the second stability in the ATF equilibria against the instability. It is reported that this tendency of the second stability is consistent with the Mercier criterion diagram in the theoretical prediction.

In the case of the Heliotron E plasma, a sawtooth crash was observed in the experiment and the mechanism of the phenomenon was explained precisely by the non-linear simulation results[90]. The sawtooth crash shown in Fig.4.1.2, was observed when

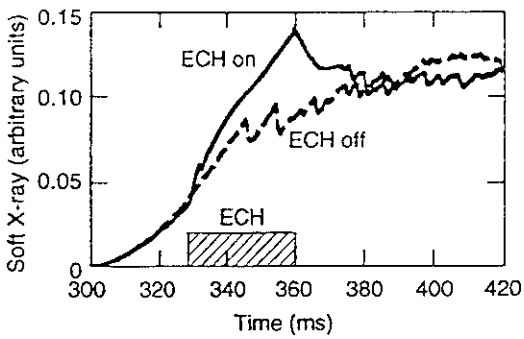

Fig.4.1.2 Line integrated soft X-ray emissivity for the two types of discharges, with and without application of ECH in the inward-shifted Heliotron E plasma. In the case of addition of ECH, the sawtooth oscillations are suppressed. [90]

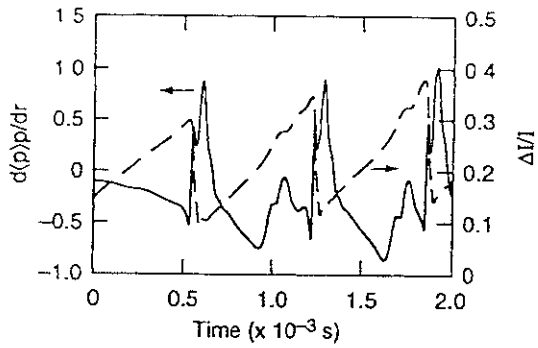

Fig.4.1.3 Time evolution of $\Delta I/I$ and the local (at $r/a = 0.15$) averaged pressure gradient for an initial equilibrium with $P = P_0(1 - \Psi_{eq})^{4.5}$ in inward-shifted Heliotron E configuration. A source term has been included to simulate sawtooth oscillation. [90]

the plasma was shifted inward with the vertical field control so that the rotational transform at the axis should be slightly less than 0.5. In this case, the surface with $\iota = 1/2$ exists in the plasma column. The position of the crash which is $r/a \simeq 0.15$ in the average radius corresponds to the $\iota = 1/2$ surface, and the poloidal mode number was identified to $m = 2$ with the technique of the tomography. The sawtooth was suppressed by applying the additional electron cyclotron resonance heating (ECH). In order to know the mechanism of this phenomenon the non-linear evolution of the fluctuation was simulated numerically by using the reduced MHD equations in the cylindrical geometry. These equations includes the resistivity, the viscosity and the heat conductivity and are solved with an additional equation for the evolution of the average pressure $\langle P \rangle$, given by,

$$\frac{\partial \langle P \rangle}{\partial t} = -\frac{\partial}{\partial r}\langle v_r P \rangle + S(r) + D_{0\perp}\frac{1}{r}\frac{\partial}{\partial r}\left(r\frac{\partial \langle P \rangle}{\partial r}\right), \tag{4.1}$$

where the bracket means the average in both the poloidal and the toroidal directions, and $S(r)$ is a source term which is needed to simulate sawtooth oscillations. The equilibrium was calculated by the VMEC code with $P = P_0(1 - \Psi_{eq})^{4.5}$ under the currentless condition. As the beta value increases, the resistive interchange mode with $m = 4/n = 2$ becomes unstable at first, but the mode saturates at a low fluctuation level. When the beta value exceeds the threshold value for the ideal interchange mode, the $m = 2/n = 1$ mode is destabilized which results in the sudden crash. Fig.4.1.3 shows the time evolution of the average pressure gradient and the soft X-ray emissivity which is estimated by

$$\frac{\Delta I}{I} = \frac{\int dl P^2 - \int dl P_{eq}^2}{\int dl P^2}, \tag{4.2}$$

where $\int dl$ means the line integral across the plasma. A good agreement of the situation of the sawtooth crash can be seen between the experimental and the numerical results, although the time evolution is accelerated by employing a larger heating source term S than the realistic value to save the computation time. Thus, the simulation showed that the ideal interchange mode triggers the crash rather than the resistive mode as the mechanism of the observed sawtooth oscillation.

In the CHS plasma, the beta value was achieved experimentally which is higher than the critical beta predicted theoretically[91]. Figure 4.1.4 shows the Mercier unstable region corresponding to the high beta experiments in the CHS. The equilibrium is calculated with the VMEC code under the currentless condition. The pressure profile observed experimentally at $\langle \beta \rangle = 0.7\%$ is used in the equilibrium calculation. This diagram predicts that the interchange mode which is resonant at the $\iota = 1/3$ surface becomes unstable and the RESORM code gives an $m = 3/n = 1$ interchange instability with substantial growth rate. On the contrary, the amplitude of $m = 3/n = 1$ component in the magnetic fluctuation was not considerable compared with $m = 2/n = 1$ in the experiment. Besides, the highest beta value in the CHS experiments, $\langle \beta \rangle = 2.1\%$, was achieved. It can be considered from these results that some stabilizing effects worked on the interchange mode.

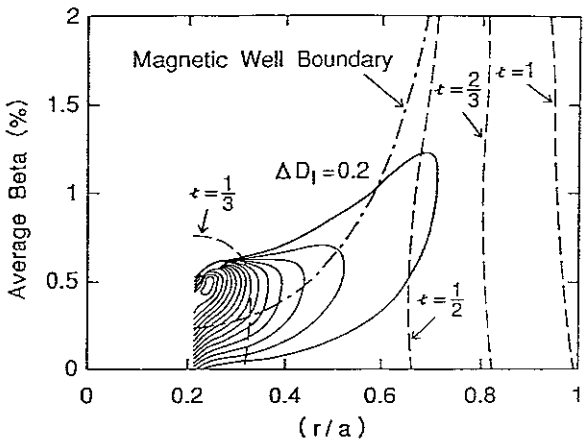

Fig.4.1.4 Mercier stability diagram in CHS plasma. The region surrounded by a thick solid line is Mercier unstable region. The thin lines are contours of the level surface of D_I with $\Delta D_I = 0.2$. [91]

The most plausible stabilizing effects are kinetic effects such as the finite Larmor radius effect. However, this effects are common in other heliotron plasmas in which the theory shows good agreements with the experimental data. Another candidate for the stabilization is the effect of the dissipations such as the viscosity and the heat conductivity. The CHS plasma is strongly heated by the neutral beam injection. The substantial anisotropy in the pressure due to the heating is observed which results in the strong viscosity. Furthermore, the CHS plasma corresponding to Fig.4.1.4 attached to the vacuum chamber, that is, the discharge was carried out in the limiter configuration with the wall. Thus, the impurity could easily come into the core plasma from the wall material which might enhance the heat conductivity across the plasma as the result of the radiation loss. It is known that such dissipation effects can stabilize the interchange mode[92]. Since the precise qualitative comparison has not been carried out, however, the disagreement between the theory and the experiment is still an open question.

5 Summary

In this review, we mainly focused on the three-dimensional MHD equilibria and its linear stability in heliotron plasmas. In this case, the interchange mode is the most basic instability because the helical windings which is necessary to generate confinement magnetic field inherently create the unfavorable curvature of the magnetic field line. This is clearly shown by the term of $|\boldsymbol{B} - \overline{\boldsymbol{B}}|^2$ in the expression of the curvature term of the stellarator expansion. The interchange mode is strongly influenced by the change of the magnetic configuration, particularly, the horizontal position controlled by the vertical field. However, it is difficult to achieve a favorable configuration both for the MHD stability against the interchange mode and for the confinement of the particles with respect to the orbit loss. Thus, it has been continued to study the stability boundary with respect to the interchange mode for various configurations and improve the compatible configuration for both the stability and the confinement. Simultaneously, the theoretical investigation for the feature of the interchange mode itself has been progressed. It is one of the great results of such investigation that the interchange mode becomes to show a ballooning feature due to the three-dimensional local magnetic curvature as the wave length decreases.

The effects of the net toroidal current on the MHD equilibrium and the stability has been studied extensively, because such net current can flow in the plasma automatically or can be induced artificially. As the net toroidal current varies the poloidal magnetic field directly, it affects the stability of the interchange mode. The effects strongly depend on the direction of the current through the change of the self-stabilization at finite beta. On the other hand, the current can cause the current driven mode. If the current density profile is peaked at the magnetic axis, as is in the case of the Ohmic current, an equilibrium involving two resonant surfaces with the same rotational transform is obtained. In this case, the internal kink mode can be unstable at low beta. When the self-consistent bootstrap current flows in the plasma column, the external kink mode is destabilized at the beta where the sufficient current flows. Another type of external mode can be found also in the current-less equilibrium at high beta, which is driven by the Pfirsch-Schlüter current.

The future work of the theoretical MHD study in the heliotron configuration which will be needed to understand the experiments more precisely is classified into two directions. One is the development of the analysis within the framework of the MHD and the other is the extension of the MHD model. In both cases, the development of the three-dimensional anal-

ysis will be important because the computer capacity has been and will be remarkably advanced.

As for the development within the MHD, the three-dimensional linear stability analysis for the resistive interchange mode as well as the ideal one should be established. The resistive stability in heliotron configurations has been studied only with the two-dimensional technique based on the stellarator expansion or other averaging methods. It will be fruitful to investigate the three-dimensional behavior of the resistive modes. Such study may reveal a special property of the resistive modes inherently in the three-dimensional configuration as is in the case of the ideal interchange mode. For the ideal stability, the three-dimensional codes such as the CAS3D and the TERPSICHORE codes are developed, however, the technique in the codes cannot be utilized in the development of the resistive stability code because they employ the energy principle. The numerical scheme based on the full MHD equations or the three-dimensional reduced MHD equations is needed for the study of the resistive instability. Some models of three-dimensional reduced equations has been proposed recently[93, 94].

Furthermore, it would be desirable to develop non-linear codes which study how much the linear instability deteriorates the plasma confinement actually. One-dimensional codes are used in the analysis of the mechanism of the destruction of the confinement region, however, the application range is limited. The toroidal effect has to be included in the non-linear studies for the small or medium aspect ratio plasma. Concerning with the achievement of a high β plasma in experiments, it is crucial whether the linear instability results in the global destruction or it locally saturates within a small level. Therefore, it would be important to generate a stability criterion so as to give the information of the the non-linear behavior of the mode and to know how well the linear stability criterion can predict the total situation of the plasma.

The analysis of the plasma with anisotropic pressure profile and plasma flow is also important in the MHD study. Although the study of these effects has been proceeded, they are limited in the one- or two-dimensional configuration. To investigate such effect in the heliotron plasma, it would be needed at first to develop a numerical code which calculates the three-dimensional MHD equilibrium consistently including the effects of the anisotropic pressure and the plasma flow.

The most important extension of the MHD model is the connection with the neoclassical transport theory. As one of the success in such extension, the self-consistent bootstrap current is incorporated in the three-dimensional equilibrium. However, the applicable plasma is limited because it is assumed that the plasma consists of the protons and the electrons and the effects of the impurity are neglected. Hence, the scheme should be modified to treat the plasma with $Z_{eff} > 1$ to analyse the experimental data closely. Furthermore, not only the bootstrap current but another neoclassical toroidal current can flow in the plasma. Particularly, in the case of the strong NBI heating, substantial beam current may flow. It has a different profile of the current density from the bootstrap current. Therefore, the scheme including the self-consistent beam current should also be established.

Including the kinetic effects are also the future problem in the three-dimensional MHD analysis. The finite Larmor radius effect is one of the most important issues in the MHD stability, particularly in the interchange mode. Because it is extremely localized around the rational surfaces near the stability boundary, it is expected that the effect would improve the stability. Thus, the development of the numerical code to study the effect on the instabilities in a three-dimensional equilibrium would be desirable. Another kinetic effect plays an important role also in the analysis of Alfvén eigenmodes. In heliotron configurations, not only the toroidicity induced Alfvén eigenmodes but also the helicity induced Alfvén eigenmodes are theoretically predicted[95] though they were not picked up in this review. However, the analysis treats the behavior of the mode only in the region of the stable eigenvalue. It would be interesting to study how such eigenmodes are destabilized by including the kinetic effects in the heliotron configurations as is done in tokamaks.

Acknowledgments

This work is partly supported by a Grant-in-Aid from the Ministry of Education, Science, Sports and Culture in Japan.

References

[1] A.Gibson, JET team, Phys. Plasmas **5** (1998) 1839.

[2] K.McGuire, H.Adler, P.Alling, et al., Phys. Plasmas **2** (1995) 2176.

[3] Y.Shimomura, R.Aymer, V.Chuyanov, M.Huguet, R.Parker and the ITER Joint Central Team and Home Teams, in Proc, IAEA Fusion Energy Conference, Yokohama, 1989, ITERP1/00.

[4] K.Uo, J. Phys. Soc. Jpn. **16** (1961) 1380.

[5] K.Uo, A.Iiyoshi, Sh.Yoshioka, T.Ishida, Sh.Konoshima, M.Sato, in Plasma Physics and Cotrolled Nuclear Fusion Research, Vienna, vol.3, (1979) 109.

[6] S.Morimoto, N.Yanagi, M.Nakasuga, T.Ohbiki, A.Iiyoshi, K.Uo, Nucl. Fusion **28** (1988) 1491.

[7] T.Obiki, M.Wakatani, et al., Fusion Tech. **17** (1990) 101.

[8] J.F.Lyon, G.L.Bell, J.D.Bell, et al., Fusion Tech. **17** (1990) 33.

[9] V.E.Bykov, A.V.Georgievskij, V.V.Demchenko, et al., Fusion Tech. **17** (1990) 140.

[10] K.Nishimura, K.Matsuoka, M.Fujiwara, et al., Fusion Tech. **17** (1990) 86.

[11] B.A.Carreras, G.Grieger, J.H.Harris, et al., Nucl. Fusion **28** (1988) 1613.

[12] A.Iiyoshi, M.Fujiwara, O.Motojima, N.Oyabu, K.Yamazaki, Fusion Tech. **17** (1990) 169.

[13] A.Iiyoshi, K.Yamazaki, Phys. Plasmas **2** (1995) 2349.

[14] A.Iiyoshi, A.Komori, et al., in Proc, IAEA Fusion Energy Conference, Yokohama, 1998, IAEA-CN-69.

[15] J.H.Harris, O.Motojima, H.Kaneko, et al., Phys. Rev. Letters **53** (1984) 2242.

[16] J.M.Greene, J.L.Johnson, Phys. Fluids 4 (1961) 875.

[17] I.B.Bernstein, E.A.Frieman, M.D.Kruskal, R.M.Kulsrud, Proc. Roy. Soc. London, **a244** (1958) 17.

[18] J.M.Greene, J.L.Johnson, Phys. Fluids 4 (1961) 1417.

[19] H.R.Strauss, Plasma Phys. **22** (1980) 733.

[20] M.Wakatani, IEEE Trans. Plasma Sci. **PS-9** (1981) 243.

[21] G.Anania, J.L.Johnson, K.E.Weimer, Phys. Fluids **26** (1983) 2210.

[22] G.Anania, J.L.Johnson, Phys. Fluids **26** (1983) 3070.

[23] B.A.Carreras, L.Garcia, V.E.Lynch, Phys. Fluids **29** (1986) 3356.

[24] L.M.Kovrizhnykh, S.V.Shchepetov, Nucl. Fusion **23** (1983) 859.

[25] T.C.Hender, B.A.Carreras, Phys. Fluids **27** (1984) 2101.

[26] K.Ichiguchi, Y.Nakamura, M.Wakatani, N.Yanagi, S.Morimoto, Nucl. Fusion **29** (1989) 2093.

[27] Y.Nakamura, K.Ichiguchi, M.Wakatani, J.L.Johnson, J. Phys. Soc. Jpn. **58** (1989) 3157.

[28] F.Bauer, O.Betancourt, P.Garabedian, 'Magnetohydrodynamic Equilibrium and Stability of Stellarators' (Springer-Verlag, New York, 1984).

[29] M.Wakatani, K.Ichiguchi, F.Bauer, O.Betancourt, P.Garabedian, Nucl. Fusion **26** (1986) 1359.

[30] S.P.Hirshman, J.C.Whitson, Phys. Fluids **26** (1983) 3553.

[31] S.P.Hirshman, W.I.van Rij, P.Merkel, Comp. Phys. Comm. **43** (1986) 143.

[32] Y.Nakamura, M.Wakatani, K.Ichiguchi, J. Plasma Fusion Res. **69** (1993) 41.

[33] K.Ichiguchi, Y.Nakamura, M.Wakatani, Nucl. Fusion **31** (1991) 2073.

[34] L.Garcia, B.A.Carreras, N.Dominguez, J.N.Lebouef, V.E.Lynch, Phys. Fluids **B2** (1990) 2162.

[35] S.A.Galkin, V.V.Drozdov, A.A.Martinov, Keldysh Institute of Applied Mathematics Preprint KIAM, No.52, 1991.

[36] Y.Nakamura, T.Matsumoto, M.Wakatani, et al., J. Comp. Phys. **128** (1996) 43.

[37] C.Schwab, Phys. Fluids **B5** (1993) 3195.

[38] D.V.Anderson, W.A.Cooper, U.Schwenn, R.Gruber, in Proc. Joint Varenna-Lausanne International Workshop on Theory and Fusion Plasmas (Bologna, 1988) 93.

[39] K.Harafuji, T.Hayashi, T.Sato, J. Comp. Phys. **81** (1989) 169.

[40] A.Reiman, H.Greenside, Comp. Phys. Comm. **43** (1986) 157.

[41] M.D.Kruskal, R.M.Kulsrud, Phys. Fluids **1** (1958) 265.

[42] S.P.Hirshman, H.K.Meier, Phys. Fluids **28** (1985) 1387.

[43] J.L.Johnson, H.E.Dalhed, J.M.Greene, et al., J. Comp. Phys. **32** (1979) 212.

[44] C.Nührenberg, Phys. Plasmas **3** (1996) 2401.

[45] C.Nührenberg, Phys. Plasmas **6** (1998) 137.

[46] G.Y.Fu, W.A.Cooper, R.Gruber, et al., Phys. Fluids **B4** (1992) 1401.

[47] K.Ichiguchi, N.Nakajima, H.J.Gardner, Nucl. Fusion **36** (1996) 1157.

[48] C.Mercier, Nucl. Fusion Suppl. Pt.2, (1962) 801.

[49] J.L.Johnson, J.M.Greene, Plasma Phys. **9** (1967) 611.

[50] A.H.Glasser, J.M.Greene, J.L.Johnson, Phys. Fluids **18** (1975) 875.

[51] K.Ichiguchi, N.Nakajima, M.Okamoto, Y.Nakamura, M.Wakatani, Nucl. Fusion **33** (1993) 481.

[52] T.Hayashi, A.Takei, T.Sato, Plasma Phys. **B4** (1992) 1539.

[53] T.Hayashi, T.Sato, et al., Phys. Plasma **1** (1994) 3262.

[54] A.H.Boozer, Phys. Fluids **25** (1982) 520

[55] B.R Suydam, Proceedings of the Second United Nations International Conference on the Peaceful Uses of Atomic Energy, Geneva, 1958, vol.31, p.157.

[56] H.Sugama, M.Wakatani, J. Phys. Soc. Jpn. **58** (1989) 1128.

[57] Y.Nakamura, K.Ichiguchi, M.Wakatani, et al., in Proc. Joint Varenna-Lausanne International Workshop on Theory and Fusion Plasmas (Bologna, 1990) 677.

[58] K.Ichiguchi, N.Nakajima, et al., accepted in J. Plasma Fusion Res. SER. (1999).

[59] M.Fujiwara, K.Yamazaki, M.Okamoto, et al., J. Fusion Energy **15** (1996) 7.

[60] B.A.Carreras, private communication (1998).

[61] L.S.Solov'ev, V.D.Shafranov, Revs. Plasma Phys. vol.5, p.1. Consultant Bureau, New York(1970).

[62] J.L.Johnson, J.M.Greene, B.Coppi, Phys. Fluids **6** (1963) 1169.

[63] K.C.Shaing, J.D.Callen, Phys. Fluids **26** (1983) 3315.

[64] K.C.Shaing, B.A.Carreras, N.Dominguez, et al., Phys. Fluids **B1** (1989) 1663.

[65] N.Nakajima, M.Okamoto, J. Phys. Soc. Jpn. **61** (1992) 833.

[66] N.Nakajima, M.Okamoto, M.Fujiwara, Kakuyugo-Kenkyu **68** (1992) 503.

[67] S.P.Hirshman, D.J.Sigmar, Nucl. Fusion **21** (1981) 1079.

[68] K,Y.Watanabe, N.Nakajima, M.Okamoto, et al., Nucl. Fusion **35** (1995) 335.

[69] K.Watanabe, N.Nakajima, M.Okamoto, et al., Nucl. Fusion **32** (1992) 1499.

[70] K.Ichiguchi, Plasma Phys. Control. Fusion **39** (1997) 1805.

[71] R.Kanno, N.Nakajima, T.Hayashi, M.Okamoto, J. Plasma Phys. **61**,part 2 (1999) 213.

[72] M.N.Rosenbluth, R.Y.Dagazian, P.H.Rutherford, Phys. Fluids **16** (1973) 1894.

[73] T.Matsumoto, Y.Nakamura, M.Wakatani, Nucl. Fusion **36** (1996) 1571.

[74] J.L.Johnson, K.Ichiguchi, et al., Phys. Plasmas **6** (1999) 2513.

[75] G.Rewoldt, J.L.Johnson, Nucl. Fusion **24** (1984) 733.

[76] J.W.Connor, R.J.Hastie, J.B.Taylor, Proc. Roy. Soc. London, **a365** (1979) 1.

[77] R.L.Dewar, A.H.Glasser, Phys. Fluids **26** (1983) 3038.

[78] J.P.Freidberg, 'Ideal Magnetohydrodynamics', Plenum Press (New York) 1987. Phys. Fluids **26** (1983) 3038.

[79] V.D.Shafranov, Phys. Fluids **26** (1983) 357.

[80] W.A.Cooper, S.P.Hirshman, D.K.Lee, Nucl. Fusion **29** (1989) 617.

[81] N.Nakajima, Phys. Plasmas **3** (1996) 4545.

[82] K.Ichiguchi, N.Nakajima, M.Okamoto, in Proc. Joint Varenna-Lausanne International Workshop on Theory and Fusion Plasmas (Bologna, 1997) 45.

[83] N.Nakajima, K.Ichiguchi, M.Okamoto, R.L.Dewar, Fusion Energy 1996, Vienna, vol.2, 497 (1997).

[84] N.Nakajima, Phys. Plasmas **3** (1996) 4556.

[85] W.A.Cooper, D.B.Singleton, R.L.Dewar, Phys. Plasmas **3** (1996) 275.

[86] J.Chen, N.Nakajima, M.Okamoto, Phys. Plasmas **6** (1999) 1562.

[87] N.Yanagi, S.Morimoto, K.Ichiguchi, et al., Nucl. Fusion **32** (1992) 1264.

[88] S.Morimoto, N.Yanagi, K.Ichiguchi, et al., J. J. Appl. Phys. **28** (1989) L1470.

[89] J.H.Harris, M.Murakami, et al., Phys. Rev. Lett. **63** (1989) 1249.

[90] B.A.Carreras, V.E.Lynch, H.Zushi, K.Ichiguchi,M.Wakatani, Phys. Plasmas **5** (1998) 3700.

[91] S.Okamura, K.Matsuoka, K.Nishimura, et al., Plasma Physics and Controlled Nuclear Fusion Research 1994, vol.1, (IAEA, Vienna, 1995)381.

[92] K.Itoh, K.Ichiguchi, S.-I.Itoh, Phys. Fluids **B4** (1992) 2929.

[93] L.Garcia, R.Sanchez, J.A.Jimenez, J.Plasma Fusion Res. SERIES **1** (1998) 468.

[94] S.E.Kruger, C.C.Hegna, J.D.Callen, Phys. Plasmas **5** (1998) 4169.

[95] N.Nakajima, C.Z.Chen, M.Okamoto, Phys. Fluids **B4** (1992) 1115.

Recent Issues of NIFS Series

NIFS-548 J.E Rice,
Simulated Impurity Transport in LHD from MIST; May 1998

NIFS-549 M.M Skoric, T. Sato, A M Maluckov and M S Jovanovic,
On Kinetic Complexity in a Three-Wave Interaction; June 1998

NIFS-550 S Goto and S. Kida,
Passive Saclar Spectrum in Isotropic Turbulence: Prediction by the Lagrangian Direct-interaction Approximation; June 1998

NIFS-551 T Kuroda, H. Sugama, R. Kanno, M. Okamoto and W Horton,
Initial Value Problem of the Toroidal Ion Temperature Gradient Mode ; June 1998

NIFS-552 T Mutoh, R. Kumazawa, T. Seki, F. Simpo, G. Nomura, T. Ido and T Watari,
Steady State Tests of High Voltage Ceramic Feedthoughs and Co-Axial Transmission Line of ICRF Heating System for the Large Helical Device ; June 1998

NIFS-553 N. Noda, K Tsuzuki, A. Sagara, N. Inoue, T Muroga,
oronaization in Future Devices -Protecting Layer against Tritium and Energetic Neutrals-: July 1998

NIFS-554 S. Murakami and H. Saleem,
Electromagnetic Effects on Rippling Instability and Tokamak Edge Fluctuations, July 1998

NIFS-555 H Nakamura , K Ikeda and S. Yamaguchi,
Physical Model of Nernst Element; Aug. 1998

NIFS-556 H. Okumura, S. Yamaguchi, H. Nakamura, K Ikeda and K Sawada,
Numerical Computation of Thermoelectric and Thermomagnetic Effects, Aug. 1998

NIFS-557 Y Takeiri, M. Osakabe, K. Tsumori, Y Oka, O. Kaneko, E. Asano, T Kawamoto, R. Akiyama and M. Tanaka,
Development of a High-Current Hydrogen-Negative Ion Source for LHD-NBI System; Aug.1998

NIFS-558 M. Tanaka, A. Yu Grosberg and T. Tanaka,
Molecular Dynamics of Structure Organization of Polyampholytes; Sep. 1998

NIFS-559 R. Horiuchi, K. Nishimura and T. Watanabe,
Kinetic Stabilization of Tilt Disruption in Field-Reversed Configurations; Sep. 1998
(IAEA-CN-69/THP1/11)

NIFS-560 S. Sudo, K. Kholopenkov, K. Matsuoka, S. Okamura, C. Takahashi, R. Akiyama, A Fujisawa, K. Ida, H. Idei, H Iguchi, M. Isobe, S Kado, K. Kondo, S. Kubo, H Kuramoto, T. Minami, S. Morita, S Nishimura, M Osakabe, M. Sasao, B. Peterson, K. Tanaka, K. Toi and Y. Yoshimura,
Particle Transport Study with Tracer-Encapsulated Solid Pellet Injection; Oct. 1998
(IAEA-CN-69/EXP1/18)

NIFS-561 A Fujisawa, H. Iguchi, S. Lee, K. Tanaka, T Minami, Y Yoshimura, M. Osakabe, K. Matsuoka, S. Okamura, H. Idei, S. Kubo, S. Ohdachi, S. Morita, R. Akiyama, K. Toi, H. Sanuki, K. Itoh, K. Ida, A. Shimizu, S Takagi, C. Takahashi, M. Kojima, S. Hidekuma, S Nishimura, M. Isobe, A. Ejiri, N. Inoue, R. Sakamoto, Y. Hamada and M. Fujiwara,
Dynamic Behavior Associated with Electric Field Transitions in CHS Heliotron/Torsatron, Oct. 1998
(IAEA-CN-69/EX5/1)

NIFS-562 S. Yoshikawa,
Next Generation Toroidal Devices; Oct. 1998

NIFS-563 Y. Todo and T. Sato,
Kinetic-Magnetohydrodynamic Simulation Study of Fast Ions and Toroidal Alfvén Eigenmodes; Oct 1998
(IAEA-CN-69/THP2/22)

NIFS-564 T. Watari, T. Shimozuma, Y. Takeiri, R. Kumazawa, T Mutoh, M. Sato, O Kaneko, K. Ohkubo, S. Kubo, H. Idei, Y. Oka, M Osakabe, T. Seki, K. Tsumori, Y. Yoshimura, R. Akiyama, T. Kawamoto, S. Kobayashi, F. Shimpo, Y. Takita, E. Asano, S Itoh, G. Nomura, T. Ido, M. Hamabe, M. Fujiwara, A. Iiyoshi, S. Morimoto, T. Bigelow and Y P Zhao,
Steady State Heating Technology Development for LHD; Oct. 1998
(IAEA-CN-69/FTP/21)

NIFS-565 A. Sagara, K.Y. Watanabe, K. Yamazaki, O. Motojima, M. Fujiwara, O. Mitarai, S. Imagawa, H. Yamanishi, H. Chikaraishi, A. Kohyama, H. Matsui, T. Muroga, T. Noda, N. Ohyabu, T. Satow, A.A. Shishkin, S. Tanaka, T. Terai and T. Uda,
LHD-Type Compact Helical Reactors;Oct. 1998
(IAEA-CN-69/FTP/03(R)

NIFS-566 N. Nakajima, J. Chen, K. Ichiguchi and M. Okamoto,
Global Mode Analysis of Ideal MHD Modes in L=2 Heliotron/Torsatron Systems;Oct. 1998
(IAEA-CN-69/THP1/08)

NIFS-567 K. Ida, M. Osakabe, K. Tanaka, T. Minami, S. Nishimura, S. Okamura, A. Fujisawa, Y. Yoshimura, S. Kubo, R. Akiyama, D.S.Darrow, H. Idei, H. Iguchi, M. Isobe, S. Kado, T. Kondo, S. Lee, K. Matsuoka, S. Morita, I. Nomura, S. Ohdachi, M. Sasao, A. Shimizu, K. Tumon, S. Takayama, M. Takechi, S. Takagi, C. Takahashi, K. Toi and T. Watari,
Transition from L Mode to High Ion Temperature Mode in CHS Heliotron/Torsatron Plasmas;Oct. 1998
(IAEA-CN-69/EX2/2)

NIFS-568 S. Okamura, K. Matsuoka, R. Akiyama, D.S. Darrow, A. Ejiri, A. Fujisawa, M. Fujiwara, M. Goto, K. Ida H. Idei, H. Iguchi, N. Inoue, M. Isobe, K. Itoh, S. Kado, K. Khlopenkov, T. Kondo, S. Kubo, A. Lazaros, S. Lee, G. Matsunaga, T Minami, S. Morita, S Murakami, N. Nakajima, N. Nikai, S. Nishimura, I. Nomura, S. Ohdachi, K. Ohkuni, M. Osakabe, R. Pavlichenko, B. Peterson, R. Sakamoto, H. Sanuki, M. Sasao, A. Shimizu, Y. Shirai, S. Sudo, S. Takagi, C. Takahashi, S. Takayama, M. Takechi, K. Tanaka, K. Toi, K. Yamazaki, Y. Yoshimura and T. Watari,
Confinement Physics Study in a Small Low-Aspect-Ratio Helical Device CHS;Oct. 1998
(IAEA-CN-69/OV4/5)

NIFS-569 M.M. Skoric, T. Sato, A. Maluckov, M.S. Jovanovic,
Micro- and Macro-scale Self-organization in a Dissipative Plasma;Oct. 1998

NIFS-570 T. Hayashi, N. Mizuguchi, T-H. Watanabe, T. Sato and the Complexity Simulation Group,
Nonlinear Simulations of Internal Reconnection Event in Spherical Tokamak;Oct 1998
(IAEA-CN-69/TH3/3)

NIFS-571 A. Iiyoshi, A. Komori, A. Ejiri, M. Emoto, H. Funaba, M. Goto, K. Ida, H. Idei, S. Inagaki, S. Kado, O. Kaneko, K. Kawahata, S. Kubo, R. Kumazawa, S. Masuzaki, T. Minami, J. Miyazawa, T. Morisaki, S. Morita, S. Murakami, S. Muto, T. Muto, Y. Nagayama, Y. Nakamura, H. Nakanishi, K. Narihara, K. Nishimura, N. Noda, T. Kobuchi, S. Ohdachi, N. Ohyabu, Y. Oka, M. Osakabe, T. Ozaki, B.J. Peterson, A. Sagara, S. Sakakibara, R. Sakamoto, H. Sasao, M. Sasao, K. Sato, M. Sato, T. Seki, T. Shimozuma, M. Shoji, H. Suzuki, Y. Takeiri, K. Tanaka, K. Toi, T. Tokuzawa, K. Tsumori, I. Yamada, H. Yamada, S. Yamaguchi, M. Yokoyama, K.Y.Watanabe, T. Watari, R. Akiyama, H. Chikaraishi, K. Haba, S. Hamaguchi, S. Iima, S. Imagawa, N. Inoue, K. Iwamoto, S. Kitagawa, Y. Kubota, J. Kodaira, R. Maekawa, T. Mito. T. Nagasaka, A. Nishimura, Y. Takita, C. Takahashi, K. Takahata, K. Yamauchi, H. Tamura, T. Tsuzuki, S. Yamada, N. Yanagi, H. Yonezu, Y. Hamada, K. Matsuoka, K. Murai, K. Ohkubo, I. Ohtake, M. Okamoto, S. Sato, T. Satow, S. Sudo, S. Tanahashi, K. Yamazaki, M. Fujiwara and O. Motojima,
An Overview of the Large Helical Device Project; Oct. 1998
(IAEA-CN-69/OV1/4)

NIFS-572 M. Fujiwara, H. Yamada, A. Ejiri, M. Emoto, H. Funaba, M. Goto, K. Ida, H. Idei, S. Inagaki, S. Kado, O. Kaneko, K. Kawahata, A. Komori, S. Kubo, R. Kumazawa, S. Masuzaki, T. Minami, J. Miyazawa, T. Morisaki, S. Morita, S. Murakami, S. Muto, T. Muto, Y. Nagayama, Y. Nakamura, H. Nakanishi, K. Nanhara, K. Nishimura, N. Noda, T. Kobuchi, S. Ohdachi, N. Ohyabu, Y. Oka, M. Osakabe, T. Ozaki, B. J. Peterson, A. Sagara, S. Sakakibara, R. Sakamoto, H. Sasao, M. Sasao, K. Sato, M. Sato, T. Seki, T. Shimozuma, M. Shoji, H. Sazuki, Y. Takeiri, K. Tanaka, K. Toi, T. Tokuzawa, K. Tsumori, I. Yamada, S. Yamaguchi, M. Yokoyama, K.Y. Watanabe, T. Watari, R. Akiyama, H. Chikaraishi, K. Haba, S. Hamaguchi, M. Iima, S. Imagawa, N. Inoue, K. Iwamoto, S. Kitagawa, Y. Kubota, J. Kodaira, R. Maekawa, T. Mito, T. Nagasaka, A. Nishimura, Y. Takita, C. Takahashi, K. Takahata, K. Yamauchi, H. Tamura, T. Tsuzuki, S. Yamada, N. Yanagi, H. Yonezu, Y. Hamada, K. Matsuoka, K. Murai, K. Ohkubo, I. Ohtake, M. Okamoto, S. Sato, T. Satow, S. Sudo, S. Tanahashi, K. Yamazaki, O. Motojima and A. Iiyoshi,
Plasma Confinement Studies in LHD; Oct. 1998
(IAEA-CN-69/EX2/3)

NIFS-573 O. Motojima, K. Akaishi, H. Chikaraishi, H. Funaba, S. Hamaguchi, S. Imagawa, S. Inagaki, N. Inoue, A. Iwamoto, S. Kitagawa, A. Komori, Y. Kubota, R. Maekawa, S. Masuzaki, T. Mito, J. Miyazawa, T. Morisaki, T. Muroga, T. Nagasaka, Y Nakmura, A. Nishimura, K. Nishimura, N. Noda, N. Ohyabu, S. Sagara, S. Sakakibara, R. Sakamoto, S. Satoh, T. Satow, M. Shoji, H. Suzuki, K. Takahata, H. Tamura, K. Watanabe, H. Yamada, S. Yamada, S. Yamaguchi, K. Yamazaki, N. Yanagi, T. Baba, H. Hayashi, M. Iima, T. Inoue, S. Kato, T Kato, T. Kondo, S. Monuchi, H. Ogawa, I. Ohtake, K. Ooba, H. Sekiguchi, N. Suzuki, S. Takami, Y. Taniguchi, T. Tsuzuki, N. Yamamoto, K. Yasui, H. Yonezu, M. Fujiwara and A. Iiyoshi,
Progress Summary of LHD Engineering Design and Construction; Oct. 1998
(IAEA-CN-69/FT2/1)

NIFS-574 K. Toi, M. Takechi, S. Takagi, G. Matsunaga, M. Isobe, T. Kondo, M. Sasao, D.S. Darrow, K. Ohkuni, S. Ohdachi, R. Akiyama A. Fujisawa, M. Gotoh, H. Idei, K. Ida, H. Iguchi, S. Kado, M. Kojima, S. Kubo, S. Lee, K. Matsuoka, T. Minami, S. Morita, N. Nikai, S. Nishimura, S. Okamura, M. Osakabe, A. Shimizu, Y. Shirai, C. Takahashi, K. Tanaka, T. Watari and Y. Yoshimura,
Global MHD Modes Excited by Energetic Ions in Heliotron/Torsatron Plasmas;Oct. 1998
(IAEA-CN-69/EXP1/19)

NIFS-575 Y. Hamada, A. Nishizawa, Y. Kawasumi, A. Fujisawa, M. Kojima, K. Narihara, K. Ida, A. Ejiri, S. Ohdachi, K. Kawahata, K. Toi, K. Sato, T. Seki, H. Iguchi, K. Adachi, S. Hidekuma, S.Hirokura, K. Iwasaki, T. Ido, R. Kumazawa, H. Kuramoto, T. Minami, I.. Nomura, M. Sasao, K.N. Sato, T. Tsuzuki, I. Yamada and T. Watari,
Potential Turbulence in Tokamak Plasmas;Oct. 1998
(IAEA-CN-69/EXP2/14)

NIFS-576 S Murakami, U. Gasparino, H. Idei, S Kubo, H Maassberg, N Marushchenko, N Nakajima, M. Romé and M Okamoto,
5D Simulation Study of Suprathermal Electron Transport in Non-Axisymmetric Plasmas;Oct. 1998
(IAEA-CN-69/THP1/01)

NIFS-577 S Fujiwara and T Sato,
Molecular Dynamics Simulation of Structure Formation of Short Chain Molecules; Nov 1998

NIFS-578 T Yamagishi,
Eigenfunctions for Vlasov Equation in Multi-species Plasmas Nov 1998

NIFS-579 M. Tanaka, A. Yu Grosberg and T Tanaka,
Molecular Dynamics of Strongly-Coupled Multichain Coulomb Polymers in Pure and Salt Aqueous Solutions, Nov 1998

NIFS-580 J. Chen, N. Nakajima and M. Okamoto,
Global Mode Analysis of Ideal MHD Modes in a Heliotron/Torsatron System. I. Mercier-unstable Equilibria, Dec 1998

NIFS-581 M Tanaka, A Yu Grosberg and T. Tanaka,
Comparison of Multichain Coulomb Polymers in Isolated and Periodic Systems: Molecular Dynamics Study; Jan 1999

NIFS-582 V.S. Chan and S. Murakami,
Self-Consistent Electric Field Effect on Electron Transport of ECH Plasmas; Feb. 1999

NIFS-583 M Yokoyama, N. Nakajima, M Okamoto, Y Nakamura and M. Wakatani,
Roles of Bumpy Field on Collisionless Particle Confinement in Helical-Axis Heliotrons;Feb. 1999

NIFS-584 T.-H. Watanabe, T. Hayashi, T. Sato, M. Yamada and H. Ji,
Modeling of Magnetic Island Formation in Magnetic Reconnection Experiment;Feb. 1999

NIFS-585 R. Kumazawa, T. Mutoh, T. Seki, F. Shinpo, G. Nomura, T. Ido, T. Watari, Jean-Marie Noterdaeme and Yangping Zhao,
Liquid Stub Tuner for Ion Cyclotron Heating;Mar. 1999

NIFS-586 A. Sagara, M. Iima, S. Inagaki, N. Inoue, H. Suzuki, K. Tsuzuki, S. Masuzaki, J. Miyazawa, S. Morita, Y Nakamura, N. Noda, B. Peterson, S Sakakibara, T. Shimozuma, H. Yamada, K. Akaishi, H Chikaraishi, H. Funaba, O Kaneko, K Kawahata, A Komori, N. Ohyabu, O. Motojima, LHD Exp. Group 1, LHD Exp. Group 2,
Wall Conditioning at the Starting Phase of LHD, Mar 1999

NIFS-587 T. Nakamura and T. Yabe,
Cubic Interpolated Propagation Scheme for Solving the Hyper-Dimensional Vlasov-Poisson Equation in Phase Space;Mar 1999

NIFS-588 W.X. Wnag, N. Nakajima, S. Murakami and M. Okamoto,
An Accurate δf Method for Neoclassical Transport Calculation;Mar 1999

NIFS-589 K. Kishida, K. Araki, S. Kishiba and K. Suzuki,
Local or Nonlocal? Orthonormal Divergence-free Wavelet Analysis of Nonlinear Interactions in Turbulence, Mar 1999

NIFS-590 K Araki, K. Suzuki, K. Kishida and S. Kishiba,
Multiresolution Approximation of the Vector Fields on T^3;Mar. 1999

NIFS-591 K. Yamazaki, H. Yamada, K Y.Watanabe, K. Nishimura, S Yamaguchi, H. Nakanishi, A. Komori, H. Suzuki, T. Mito, H Chikaraishi, K. Murai, O Motojima and the LHD Group,
Overview of the Large Helical Device (LHD) Control System and Its First Operation, Apr. 1999

NIFS-592 T. Takahashi and Y. Nakao,
Thermonuclear Reactivity of D-T Fusion Plasma with Spin-Polarized Fuel; Apr. 1999

NIFS-593 H. Sugama,
Damping of Toroidal Ion Temperature Gradient Modes, Apr. 1999

NIFS-594 Xiaodong Li,
Analysis of Crowbar Action of High Voltage DC Power Supply in the LHD ICRF System; Apr 1999

NIFS-595 K. Nishimura, R. Horiuchi and T. Sato,
Drift-kink Instability Induced by Beam Ions in Field-reversed Configurations; Apr. 1999

NIFS-596 Y. Suzuki, T-H. Watanabe, T. Sato and T. Hayashi,
Three-dimensional Simulation Study of Compact Toroid Plasmoid Injection into Magnetized Plasmas; Apr. 1999

NIFS-597 H. Sanuki, K. Itoh, M. Yokoyama, A. Fujisawa, K. Ida, S. Toda, S.-I. Itoh, M. Yagi and A. Fukuyama,
Possibility of Internal Transport Barrier Formation and Electric Field Bifurcation in LHD Plasma, May 1999

NIFS-598 S. Nakazawa, N. Nakajima, M. Okamoto and N. Ohyabu,
One Dimensional Simulation on Stability of Detached Plasma in a Tokamak Divertor; June 1999

NIFS-599 S. Murakami, N. Nakajima, M. Okamoto and J Nhrenberg,
Effect of Energetic Ion Loss on ICRF Heating Efficiency and Energy Confinement Time in Heliotrons; June 1999

NIFS-600 R. Horiuchi and T. Sato,
Three-Dimensional Particle Simulation of Plasma Instabilities and Collisionless Reconnection in a Current Sheet;; June 1999

NIFS-601 W. Wang, M. Okamoto, N. Nakajima and S. Murakami,
Collisional Transport in a Plasma with Steep Gradients; June 1999

NIFS-602 T. Mutoh, R. Kumazawa, T. Saki, K. Saito, F. Simpo, G. Nomura, T. Watari, X. Jikang, G. Cattanei, H. Okada, K. Ohkubo, M. Sato, S. Kubo, T Shimozuma, H. Idei, Y. Yoshimura, O. Kaneko, Y. Takeiri, M. Osakabe, Y. Oka, K. Tsumori, A. Komori, H. Yamada, K. Watanabe, S. Sakakibara, M. Shoji, R. Sakamoto, S. Inagaki, J. Miyazawa, S. Morita, K. Tanaka, B.J. Peterson, S. Murakami, T. Minami, S. Ohdachi, S. Kado, K. Narihara, H. Sasao, H. Suzuki, K. Kawahata, N. Ohyabu, Y. Nakamura, H. Funaba, S. Masuzaki, S. Muto, K. Sato, T. Morisaki, S. Sudo, Y. Nagayama, T. Watanabe, M. Sasao, K.. Ida, N. Noda, K. Yamazaki, K. Akaishi, A. Sagara, K. Nishimura, T. Ozaki, K. Toi, O. Motojima, M. Fujiwara, A. Iiyoshi and LHD Exp. Group 1 and 2,
First ICRF Heating Experiment in the Large Helical Device; July 1999

NIFS-603 P.C. de Vries, Y. Nagayama, K. Kawahata, S. Inagaki, H. Sasao and K. Nagasaki,
Polarization of Electron Cyclotron Emission Spectra in LHD; July 1999

NIFS-604 W. Wang, N. Nakajima, M. Okamoto and S. Murakami,
δf Simulation of Ion Neoclassical Transport; July 1999

NIFS-605 T. Hayashi, N. Mizuguchi, T. Sato and the Complexity Simulation Group,
Numerical Simulation of Internal Reconnection Event in Spherical Tokamak; July 1999

NIFS-606 M. Okamoto, N. Nakajima and W. Wang,
On the Two Weighting Scheme for δf Collisional Transport Simulation; Aug. 1999

NIFS-607 O. Motojima, A.A. Shishkin, S. Inagaki, K. Y. Watanabe,
Possible Control Scenario of Radial Electric Field by Loss-Cone-Particle Injection into Helical Device; Aug. 1999

NIFS-608 R. Tanaka, T. Nakamura and T. Yabe,
Constructing Exactly Conservative Scheme in Non-conservative Form; Aug. 1999

NIFS-609 H. Sugama,
Gyrokinetic Field Theory; Aug. 1999

NIFS-610 M. Takechi, G. Matsunaga, S. Takagi, K.Ohkuni, K. Toi, M. Osakabe, M. Isobe, S. Okamura, K. Matsuoka, A. Fujisawa, H. Iguchi, S. Lee, T. Minami, K. Tanaka, Y. Yoshimura and CHS Group,
Core Localized Toroidal Alfven Eigenmodes Destabilized By Energetic Ions in the CHS Heliotron/Torsatron; Sep. 1999

NIFS-611 K. Ichiguchi,
MHD Equilibrium and Stability in Heliotron Plasmas; Sep. 1999